Electronic Supplementary Information

Selective solar driven CO_2 reduction to hydrocarbons

Gurudayal,[1,2,3] James Bullock,[4,5] Dávid F. Srankó,[1,6] Clarissa M. Towle,[3,5] Yanwei Lum,[1,3,5] Mark Hettick,[4,5] M. C. Scott[3,7] Ali Javey,[4,5] and Joel Ager[1,2,3,5]

[1]Joint Center for Artificial Photosynthesis, Lawrence Berkeley National Laboratory, 1 Cyclotron Road, Berkeley, CA 94720, USA

[2]Chemical Sciences Division, Lawrence Berkeley National Laboratory, 1 Cyclotron Road, Berkeley, CA 94720, USA

[3]Department of Materials Science and Engineering, University of California Berkeley, Berkeley, CA 94720, USA

[4]Department of Electrical Engineering and Computer Science, University of California Berkeley, Berkeley, CA 94720, USA

[5]Materials Sciences Division, Lawrence Berkeley National Laboratory, 1 Cyclotron Road, Berkeley, CA 94720, USA

[6]Hungarian Academy of Sciences Centre for Energy Research, Surface Chemistry and Catalysis Department, Konkoly-Thege Miklós út 29-33, H-1121 Budapest, Hungary

[7]National Center for Electron Microscopy, Molecular Foundry, Lawrence Berkeley National Laboratory, Berkeley CA, 94720

Correspondence and requests for materials should be addressed to J.W.A. (email: JWAger@lbl.gov).

Table of Contents

Methods

Chemicals and Materials. All materials were used as received unless otherwise specified. Cesium carbonate (Cs_2CO_3, ACS ≥99.995%) was purchased from Sigma-Aldrich. Copper foil and silver foil (0.1 mm thick, Cu and Au, each 99.999% metal basis) were purchased from Alfa Aesar. Carbon dioxide (CO_2, 99.995%), nitrogen (N_2, 99.999%), helium (He, 99.999%), and hydrogen (H_2, 99.999%) were purchased from Praxair. Electrolyte solutions were prepared with 18.2 MΩ deionized water from a Millipore system. $CsHCO_3$ electrolyte solutions (0.1–0.5 M) were prepared by vigorously bubbling (0.05–2.5 M) Cs_2CO_3 solutions with CO_2 gas for a few minutes to achieve the desired pH. Copper sulfate ($CuSO_4$, ACS ≥99.99% trace metal basis), zinc nitrate hexahydrate ($Zn(NO_3)_2{\cdot}6H_2O$, Reagent Grade ≥98%), hexamethylenetetramine ($C_6H_{12}N_4$, ACS ≥99.0%), ethanolamine (NH_2OH, ACS ≥98%), 2-Methoxyethanol ($CH_3OCH_2CH_2OH$, ≥99%), hydrogen peroxide solution (H_2O_2, 30 wt.%), oxalic acid ($C_2H_2O_4$, anhydrous, ≥99.0%), sulfuric acid (H_2SO_4, ≥99.0%), and potassium carbonate (K_2CO_3, ACS ≥99.995%, trace metal basis) were purchased from Sigma-Aldrich. Zinc acetate ($ZnC_4H_6O_4$, anhydrous, ≥99.98%, metal basis) and iridium chloride ($IrCl_4$, ≥99.95%, metal basis) were purchased from Alfa Aesar.

Cathode Preparation. Silver foil was cut into 2-cm squares and cleaned by sonication for 15 min in acetone, isopropanol, and deionized (DI) water. Silver foil electrodes were sanded with increasing grades of sandpaper from 1200 to 2500 grit and then mechanically polished with five-micron size alumina nanoparticles (TED Pella Inc, product no. 895-6-18). The mechanically-polished silver foils were degreased in 0.1 M HCl for 5 min to remove the undesired oxide layer and finally washed in DI water for 45 min. An aqueous solution of 0.1 M copper sulfate was prepared and maintained at pH 1 by adding sulfuric acid prior to electrodeposition. The nanocoral CuAg bimetallic cathode was fabricated by a two-electrode electrodeposition method. A Teflon cell was used for electrodeposition, in which the silver foil was the working electrode and a Pt mesh was used as the counter electrode. The electrodeposition process was performed at a constant current of 400 mA for 2, 10 and 60 sec. The 10 sec deposition time was found to be optimal in terms of selectivity to the target products; this condition was used throughout the study. After electrodeposition, the CuAg cathode was washed in DI water and dried with a gentle nitrogen stream. Under high current density conditions, the competitive reaction of hydrogen evolution

forms a bubble template, which defines the nanocoral morphology and also controls the amount of silver deposited at the surface.

For comparison, we synthesized an oxide-derived copper cathode following the method of Li *et al*.[27] Copper foil was cut into 2 cm squares and cleaned by degreasing for 30 min in acetone, isopropanol, and DI water. The electrodes were then electropolished in concentrated phosphoric acid at a potential of 2.0 V for 5 min with a copper-foil counter electrode. The electro-polished Cu foils were rinsed with DI water and dried with a stream of nitrogen. Finally, the Cu foils were annealed at 500 ^{o}C for 2 hrs to obtain oxide-derived copper cathodes.

IrO_2 anode preparation. We prepared high surface area IrO_2 by adapting and modifying the procedure of Zhao *et al*.[23] Instead of drop casting, we grew the sacrificial template with hydrothermal synthesis, which produced better uniformity. We performed hydrothermal growth of both TiO_2 and ZnO templates. However, we found that we were not able to completely remove the TiO_2 template after IrO_2 deposition whereas the ZnO nanorods could be etched easily with dilute perchloric acid. We prepared iridium foil and FTO-coated glass substrates by sonication for 15 min in acetone, isopropanol, and DI water. Iridium foil was prepared by sanding with increasing grades of sandpaper from 1200 to 2500 grit and then degreased in 0.1 M HCl for 5 min to remove the undesired oxide layer and finally rinsed in DI water for 45 min. FTO-coated glass substrates were ultrasonicated for 15 min in soap solution, decon solution, DI water, acetone, and 2-methoxyethanol. These substrates were dried with a nitrogen stream. The ZnO template was prepared by adapting a previously-reported two-step method.[28] First, a seed layer of ZnO was deposited by spin coating a solution of 0.1 M zinc acetate, 0.05 M ethanolamine, and 2-methoxyethanol. Two spin-coating depositions were performed: first at 500 rpm for 5 sec and then at 3000 rpm for 30 sec, followed by annealing at 350 °C for 5 min. This procedure was repeated three times to obtain the desired thickness of the ZnO seed layer. Finally, ZnO nanorods were grown on seed layer coated substrates via hydrothermal synthesis. In short, an aqueous solution of 30 mM zinc nitrate and 15 mM hexamethylenetetramine were poured into a Teflon liner with the FTO substrates and Ir foil and then heated at 95 °C for 6 hrs. Afterwards, the hydrothermally-grown ZnO nanorod samples were rinsed with DI water and blow dried with nitrogen.

The iridium oxide precursor solution was prepared in 4 steps: (i) 50 ml of 0.005 M iridium chloride aqueous solution (dark brown) was stirred for 30 min; (ii) 0.5 mL hydrogen peroxide (30 wt%) was added slowly and stirred for 15 min until the solution color turned from light brown to yellowish; (iii) 250 mg oxalic acid was mixed in the solution while, over 15 minutes, the solution turned to a light yellowish color; (iv) potassium carbonate was slowly added to change the pH to ~10. We aged the solution for three days until the solution turned a purple or blueish color. Electrodeposition of IrO_2 was performed in a three-electrode configuration, with FTO/ Ir foil used as the working electrode, Ag/AgCl as the reference electrode, and Pt wire as the counter electrode. A cyclic voltammetry scan from 0 to 0.6 V vs Ag/AgCl was repeated 30 times at a rate of 50 mV per second. After electrodeposition, the samples were soaked for 10 min in 0.01 M perchloric acid to etch the ZnO layer. Finally, the iridium oxide (IrO_2) nanotube array was washed with DI water and blow dried with nitrogen. The morphology of the IrO_2 and the absence of ZnO was confirmed with SEM and EDX measurements. We have also used different nanorods templates (TiO_2 and Fe_2O_3) with different nanorods length but found difficulty to remove these templates after IrO_2 deposition.

Testing of cathodes and anodes. The CO_2 RR activity of CuAg cathode was tested in a three-electrode configuration at a fixed potential of -1.0 V vs. RHE in 0.2 M $CsHCO_3$ electrolyte (pH = 7.1) in a sandwich-type polyether ether ketone (PEEK) cell purged with CO_2 at 5 sccm. IrO_2 and Ag/AgCl were used as counter and reference electrodes, respectively. The -1.0 V vs RHE potential was chosen based on literature values in order to optimize the C_{2+} product selectivity.[15,29,30]

Current-voltage measurements were carried out for IrO_2 nanotube anodes in a three-electrode configuration, with platinum foil as the counter electrode, Ag/AgCl as the reference electrode and IrO_2 nanotubes as the working electrode. The three-electrode J-V measurements were performed in different concentrations of $CsHCO_3$ electrolyte (0.1-0.5 M). Applied voltages vs. Ag/AgCl were converted to RHE scale using the Nernst equation. The IrO_2 nanotubes on Ir foil (Ir/IrO_2) exhibit superior performance to IrO_2 nanotubes on Ti foil (Ti/IrO_2) and to IrO_2 nanotubes on a FTO substrate.

Electrochemical cell and measurement of gas and liquid products. The compression cell and product measurement protocol used in this work have been described in detail previously;[22] therefore, a summary will be given here. We cleaned the sandwich cell in aqua regia or nitric acid

and DI water before every measurement and each measurement was repeated several times. All the gaseous products were measured with an inline GC (SRI 8610C) and liquid samples were collected after GC measurements and fed to the high-performance liquid chromatograph (HPLC) for liquid products analysis.

Power matching electronics. Coupling of two Si PV cells in series to the electrochemical cell was accomplished with an MPP tracker (Texas Instruments BQ25504EVM-674 board with integrated inductive boost converter) which, as received, can supply voltages up to 2.9 V from a minimum 0.9 V input. The output voltage was adjusted to suit our target voltage range by replacing the fixed feedback resistor (5.9 MΩ) on the board with an adjustable potentiometer (3-7 MΩ).

The four terminal III-V/ Si tandem solar cells were interfaced to two modified MPP trackers. One MPP tracker was connected with two outer (top) series-connected III-V absorbers, while other MPP tracker was connected to the two bottom Si absorbers. These two MPP circuits were connected in parallel to each other and to the electrochemical cell to provide constant voltage. We used two MPP trackers to avoid spectrum mismatch between the top and bottom absorbers (See solar to hydrocarbons discussion in the SI for details).

Solar-driven CO_2 reduction cell. Solar-driven measurements of TD1 and TD2 were conducted by a calibrated xenon lamp equipped with AM 1.5G and AM0 filters. Optical neutral density filters were used to control the illumination intensities (See solar to hydrocarbons in supporting info for details). A pyranometer (SolarLight Co. Inc., Model: PMA2144) was used to calibrate the power density for different optical density filter configurations. A certified silicon solar cell (Newport, Model:91150V) was used to calibrate the light intensity. CO_2 was purged continuously at a rate of 5 sccm during the measurement.

Calculation of standard potentials for CO_2 reduction reactions

Table S2. Standard Gibbs free energies of formation, enthalpies of formation, and standard entropies for the chemical species of interest.[5,6]

IUPAC Name	Common Name	Formula	$\Delta G_f°$ (kJ/mol)	$\Delta H_f°$ (kJ/mol)	$S°$ $(J/mol{\cdot}K)$
Carbon dioxide	--	$CO_2\,(g)$	-394.	-393.5	213.8
Carbon monoxide	--	$CO\,(g)$	-137.0	-110.5	197.7
Methanoic acid	Formic acid	$CHOOH\,(l)$	-362.4	-426.	131.8
Methanoate	Formate	$CHOO^-\,(aq)$	-341.0	-426.0	57.16
Methanol	--	$CH_3OH\,(l)$	-166.0	-238.4	127.2
Methane	--	$CH_4\,(g)$	-51.22	-74.87	188.3
Ethane	--	$C_2H_6\,(g)$	-31.7	-84.	229.1
Ethene	Ethylene	$C_2H_4\,(g)$	68.7	52.47	219.3
Ethanal	Acetaldehyde	$CH_3CHO\,(l)$	-119.2	-196.4	117.3
Ethanol	--	$C_2H_5OH\,(l)$	-172.5	-276.	159.9
Ethane-1,2-diol	Ethylene glycol	$C_2H_6O_2\,(l)$	-328.	-460	166.9
Propan-1-ol	Propanol	$C_3H_7OH\,(l)$	-168.	-302.5	192.8
Propanal	Propionaldehyde	$C_3H_6O\,(l)$	-128.7	-218.3	212.9
Prop-2-en-1-ol	Allyl alcohol	$C_3H_5OH\,(l)$	-73.9	-171.1	187.4
1-Hydroxypropan-2-one	Hydroxyacetone	$C_3H_6O_2\,(l)$	-298	-414.2	226.1

For chemical species of interest (Table S2), the standard thermodynamic quantities of enthalpy of formation, $\Delta H_f°$, and entropy, $S°$, were obtained from the National Institute of Standards and Technology (NIST) database where possible, and the Design Institute for Physical Property Research (DIPPR) Project 801 database otherwise[5,6]. The standard Gibbs free energy of formation, $\Delta G_f°$, was then calculated for each species per the following fundamental equation:

$$\Delta G^\circ = \Delta H^\circ - T\,\Delta S^\circ \quad \text{(S1)}$$

where *T* is the standard temperature, 298.2 K, and ΔS° is the change in standard entropy for the formation reaction of each chemical species. For example, to obtain the ΔS° relevant to the formation of carbon dioxide, an equation is formulated from the chemical equation as shown below:

$$C_{(s)} + O_{2(g)} \rightarrow CO_{2(g)}$$
$$\Delta S^\circ_{reaction} = \Sigma S^\circ_{products} - \Sigma S^\circ_{reactants} \quad \text{(S2)}$$
$$\Delta S^\circ_{CO_{2(g)}} = S^\circ_{CO_{2(g)}} - (S^\circ_{C_{(s)}} + S^\circ_{O_{2(g)}})$$

The values $S^\circ_{CO_{2(g)}}$, $S^\circ_{C_{(s)}}$ (where $C_{(s)}$ is graphite), and $S^\circ_{O_{2(g)}}$ were obtained from the NIST database[5] and used to calculate $\Delta S^\circ_{CO_{2(g)}}$ as shown:

$$\Delta S^\circ_{CO_{2(g)}} = S^\circ_{CO_{2(g)}} - \left(S^\circ_{C_{(s)}} + S^\circ_{O_{2(g)}}\right)$$
$$= 213.795\ \frac{J}{mol\cdot K} - (6.201 + 205.15)\ \frac{J}{mol\cdot K} = 2.44\ \frac{J}{mol\cdot K}$$

This ΔS° was subsequently utilized, together with the ΔH_f° value from the NIST database, to calculate the ΔG_f° using Eq. S1:

$$\Delta G_f^\circ = \Delta H_f^\circ - T\,\Delta S^\circ = -393.51\ \frac{kJ}{mol} - (298.2\ K)\left(2.44\ \frac{J}{mol\cdot K}\right) = -394.\ \frac{kJ}{mol}$$

For all gaseous and liquid chemical species of interest, this general method was employed to obtain the standard Gibbs free energies of formation, which will be utilized when calculating electrochemical potentials. CO_2 reduction reactions resulting in different products can be imagined as the combustion reactions of those products run in reverse. To this effect, the heat of combustion, ΔH_c, was found for each product and can be found in Tables S3-S5. These values were verified against published values from the NIST database. In order to calculate the heat of combustion for a reaction, the heats of formation of the combustion products are subtracted from those of the reactants in a form analogous to Eq. S2:

$$\Delta H^\circ_c = \Sigma H^\circ_{f,products} - \Sigma H^\circ_{f,reactants} \quad (S4)$$

The Gibbs free energy, ΔG_r, of each CO_2 reduction reaction was calculated using Eq. S1, where ΔS_r was obtained by Eq. S2, and where $\Delta H_r = -\Delta H_c$. Calculated ΔG_r values are listed in Tables S3-S5, along with the corresponding reactions.

Table S3. CO_2 reduction reactions and electrochemical data for single-carbon products.

Product	Overall reaction	e^-	ΔH_c (kJ/mol)	ΔG_r (kJ/mol)	$E°$ (V)	$E_{H_2}°$- $E°$ (V)
Carbon monoxide	$CO_2 \leftrightarrow CO + \frac{1}{2} O_2$	2	-283.0	257.4	1.334	-0.106
Formic acid /Formate	$CO_2 + H_2O \leftrightarrow HCOOH + \frac{1}{2} O_2$	2	-254.2	269.1	1.395	-0.166
Methanol	$CO_2 + 2\,H_2O \leftrightarrow CH_3OH + \frac{3}{2} O_2$	6	-726.8	702.6	1.214	0.014
Methane	$CO_2 + 2\,H_2O \leftrightarrow CH_4 + 2\,O_2$	8	-890.3	817.4	1.059	0.169

Table S4. CO_2 reduction reactions and electrochemical data for two-carbon products.

Product	Overall reaction	e^-	ΔH_c (kJ/mol)	ΔG_r (kJ/mol)	$E°$ (V)	$E_{H_2}°$- $E°$ (V)
Ethane	$2\,CO_2 + 3\,H_2O \leftrightarrow C_2H_6 + \frac{7}{2} O_2$	14	-1561.	1468	1.087	0.141
Ethylene	$2\,CO_2 + 2\,H_2O \leftrightarrow C_2H_4 + 3\,O_2$	12	-1411.	1332	1.150	0.078
Acetaldehyde	$2\,CO_2 + 2\,H_2O \leftrightarrow CH_3CHO + \frac{5}{2} O_2$	10	-1162.	1144	1.185	0.043
Ethanol	$2\,CO_2 + 3\,H_2O \leftrightarrow C_2H_5OH + 3\,O_2$	12	-1369.	1328	1.147	0.081
Ethylene glycol	$2\,CO_2 + 3\,H_2O \leftrightarrow C_2H_6O_2 + \frac{5}{2} O_2$	10	-1185.	1172	1.215	0.013

Table S5. CO_2 reduction reactions and electrochemical data for three-carbon products.

Product	Overall reaction	e^-	ΔH_c (kJ/mol)	ΔG_r (kJ/mol)	$E°$ (V)	$E_{H_2}°$- $E°$ (V)
Propanol	$3\,CO_2 + 4\,H_2O \leftrightarrow C_3H_8O + \frac{9}{2} O_2$	18	-2021.	1964.	1.131	0.098
Propionaldehyde	$3\,CO_2 + 3\,H_2O \leftrightarrow C_3H_6O + 4\,O_2$	14	-1820.	1766.	1.144	0.084
Allyl alcohol	$3\,CO_2 + 3\,H_2O \leftrightarrow C_3H_5OH + 4\,O_2$	16	-1867.	1821.	1.179	0.049
Hydroxyacetone	$3\,CO_2 + 3\,H_2O \leftrightarrow C_3H_6O_2 + \frac{7}{2} O_2$	16	-1624.	1597.	1.182	0.046

Standard electrochemical potentials, $E°$, are calculated from ΔG_r by the following relation:

$$E° = \frac{\Delta \mathrm{G_r}}{n\ \mathrm{F}} \tag{S5}$$

where *n* is the number of moles of electrons transferred and F is Faraday's constant, the charge of one mole of electrons (96485.3 C). These electrochemical potentials are compared to the standard potential of the reversible hydrogen electrode (RHE), which is 1.23V; their difference is listed in the final column of Tables S3-S5.

Energetic Efficiency Calculation

Calculation of the overall electrochemical cell efficiency accounts for all potential losses in the cell. Most importantly, this efficiency can only be derived from a two electrode measurement, because the potential drops at counter electrode and in the solution are, in general, unknown in the three electrode configuration. Kenis and co-workers have reviewed the energetic efficiency of a number of CO_2 electrolysis cells.[7] However, they found that many studies reported only the 3-electrode data, making quantitative comparisons between different approaches not possible.

The cell energetic efficiency can be calculated by the equation below:

$$\eta_{\mathrm{energetic}} = \frac{\sum E_i^0 \times FE_i}{\mathrm{V}_{cell}} \tag{S6}$$

where E^o is the standard thermodynamic potential of each product produced (see Tables S3-S5 for all thermodynamic potentials), FE is the Faradaic efficiency of the product, and V_{cell} is that applied without considering any IR compensation. We also prepared a table of energetic efficiency data from literature reports and compared with available data and also with selected energetic efficiency data from PV driven system, when appropriate, with our data (Table S6).

Table S6. Reported electrical energy conversion energetic efficiencies for CO_2 electrochemical reduction devices. Data is for two electrode measurements as this configuration is necessary for calculating the overall energy conversion efficiency.

Source	Cathode Anode	Electrolyte and CO_2 feed	Cell voltage Current density	Energy conversion efficiency	CO_2 RR Products	Cell Type
B A Rosen[8]	Ag Pt	Ionic liquid catholyte & 0.1 M H_2SO_4 anolyte	1.5 V cathode Not reported	87%	CO	Electrolyte flow cell
P G Russell[9]	Hg Pt	0.1 M $NaHCO_3$+ 0.02 M NaCOOH	4.31 V 1 mA cm^{-2}	45%	HCOOH	Four-compartment (3x anode, 1x cathode) cell with fine glass frits and agar as separators
T Yamamoto[10]	Ni-ACF GDE Ni foam	0.5 M $KHCO_3$	3.05 V 10 mA cm^{-2}	44.6%	CO and H_2	Electrolyte flow cell
K Wu[11]	Ag GDE Pt GDE	1 M KCl	3.0 V ~47 mA cm^{-2}	37.5%*	CO and H_2	Electrolyte flow cell
M Gratzel[12]	Au IrO_2	0.5 M $NaHCO_3$	3.1 V tandem 5.93 mA cm^{-2}	39%*	CO	EC+PV tandem cell
A David[13]	Ag NiFe	0.1 M $KHCO_3$ & 1 M NaOH	2.7 V ~9 mA cm^{-2}	37%*	CO	Two-compartment cell with bipolar membrane
X Zhou[14]	Pd/C on Ti mesh GaAs/InGaP /TiO_2/Ni	2.8 M $KHCO_3$ 1 M KOH	2.04 V PV + 1.21 V anode 8.5 mA cm^{-2}	59.3%	$HCOO^-$	Two-compartment cell with bipolar membrane and pumping electrolyte
C Delacourt[15]	Ag GDE Pt-Ir alloy	0.5 M $KHCO_3$ 1 M KOH	2–4 V 5–100 mA cm^{-2}	15 -50%	CO + H_2	Fuel-cell type, two-compartment cell with pumping electrolyte
S R Narayanan[16]	In-Pd powder Pt black	1 M $NaHCO_3$ 10wt% NaOH	~3 V 40 mA cm^{-2}	~16%*	$HCOO^-$	PEM cell
This work	Cu-Ag Nanocoral IrO_2 Nanotubes	0.1-0.5 M $CsHCO_3$, CO_2 bubbled into cell	3.5 V ~9 mA cm^{-2}	33-35%	H_2 + HCs with a majority of ethylene, ethanol, and propanol	EC+PV tandem cell
This work	Cu-Ag Nanocoral IrO_2 Nanotubes	0.1-0.5 M $CsHCO_3$, CO_2 bubbled into cell	2.5 V 6.7 mA cm^{-2}	50% for all products; 24% for HCs and oxygenates	H_2 + HCs with a majority of ethylene, ethanol, and propanol	Two-compartment sandwiched cell with anion exchange membrane

* – calculated by us

Calculation of solar to chemical product conversion efficiency

Solar-to-chemical (STC) conversion efficiency of an EC-PV tandem cell based upon sum of all products generated during catalysis, as, in principle, all could be converted back to CO_2 utilizing their free energy. STC efficiency can be calculated of individual product by knowing their standard thermodynamic potential, operating current, faradaic efficiency of that product and input solar power.

$$\eta_{\mathrm{STC}} = \sum \frac{J_{\mathrm{op}} \times E^{o} \times FE}{P_{\mathrm{in}}} \quad \text{(S7)}$$

where, J_{op} is operating current density, E^{o} is the thermodynamic potential of the respective product, FE is the Faradaic efficiency and P_{in} is input power. For example, the STC efficiency of a solar converter which produced only CO would be:

$$\eta_{\mathrm{STC,CO}} = \frac{J_{\mathrm{op}} \times 1.33 \times FE}{100 \times Area} \quad \text{(S8)}$$

SEM and EDX analysis of CuAg cathode

The microstructure of the CuAg "nanocoral" cathode is shown in the SEM image in Fig. S1. Energy dispersive X-ray spectroscopy (EDS) measurements performed in scanning electron microscope mode indicates the copper-enriched surface (Figure 2a). We performed extensive SEM-EDX measurements of CuAg cross section at two different angles, which clearly shows a distribution of copper and silver along the surface (Figure S19).

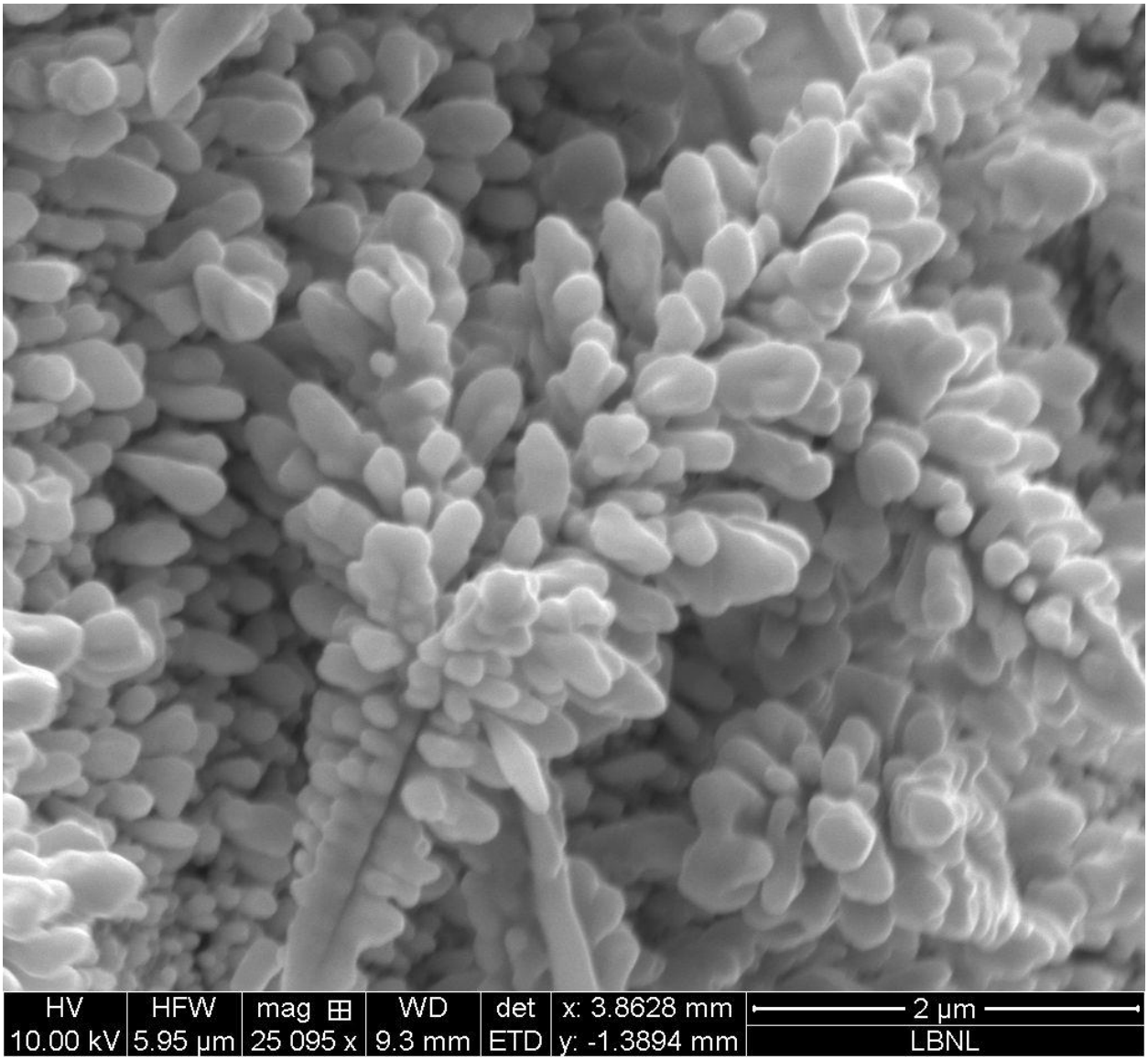

Figure S1. Surface view SEM image of bimetallic CuAg nanocoral cathode.

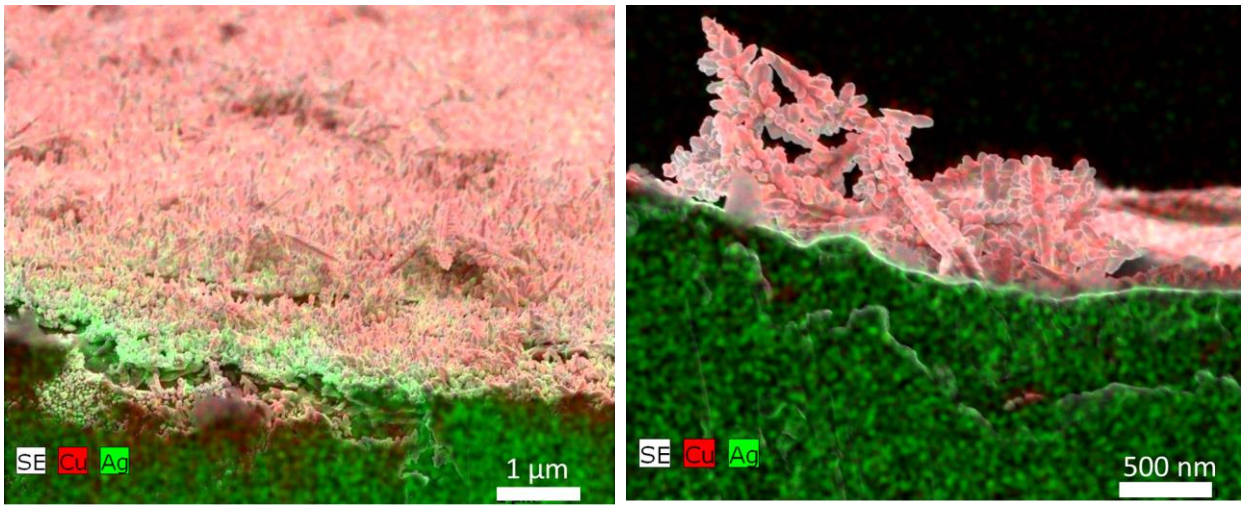

Figure S2. EDX cross section views of CuAg cathode at different tilt angles, left images was taken at 75 ^{O}C and right at 90 ^{O}C.

XRD and XPS Analysis of CuAg Cathode

The XRD patterns of the CuAg "nanocoral" cathode can be indexed to the characteristic diffraction peaks of Cu (JCPDS no. 04-003-2953), Cu_2O (JCPDS no. 04-003-6433) and Ag (JCPDS no. 04-089-3722) (Fig. S2). Both metals are polycrystalline. At different grazing incidence (0.5˚, 1.5˚, 2.5˚), two copper phases, Cu^0 and Cu_2O are observed beside the metallic silver one. The dominant reflection is related to the (111) crystal lattice in the case of Ag^0 and Cu_2O, while in the case of Cu^0 the ones indexed as (111) and (200) are both in presence with the dominance of the (111) crystal lattice.

To further investigate the composition of Cu and Ag on the surface of nanocoral sample, XPS analyses were performed (Table S1). The XPS survey scan of CuAg nanocoral cathode shows the presence of copper, silver, oxygen and carbon on the surface (Fig S3). The high resolution spectra of the characteristic lines (Cu 2p, Ag 3d, O 1s, C 1s) are shown in Fig S4 a-d. A strong peak of Cu 2p at 932.4 eV can be assigned to the Cu^0 or the Cu^{1+} state, while the shoulder appeared at 934.6 eV and the presence of the characteristic "shake up" satellite structure is typical for Cu^{2+} state.[1] The main elements of the C 1s line are related to adventitious carbon contaminations and the smaller peak appeared at 288.8 eV is related to carbon in carbonate state.[1,2] The satellites in oxygen peak could be assigned to three different chemical state, as the one at 530.4 eV is typical for oxygen in Cu_2O, while the other at 531.5 eV is characteristic for oxygen in $CuCO_3$ or $Cu(OH)_2$ state.[3,4] The third chemical state appeared at binding energy of 532.7 eV is related to oxygen in

carbonic environment (adventitious carbon contaminations). According to the surface concentrations, the presence of the Cu 2p peak at 932.4 eV with the O 1s peak at 530.4 eV is ideal for Cu_2O content, while the Cu^{2+} with O 1s peak at 531.5 eV could be assigned to copper (II) carbonate hydroxide ($Cu_2(OH)_2CO_3$) state.[2] Silver is also present on the surface in metallic state with a low atomic concentration (1 at%) (Table S1).

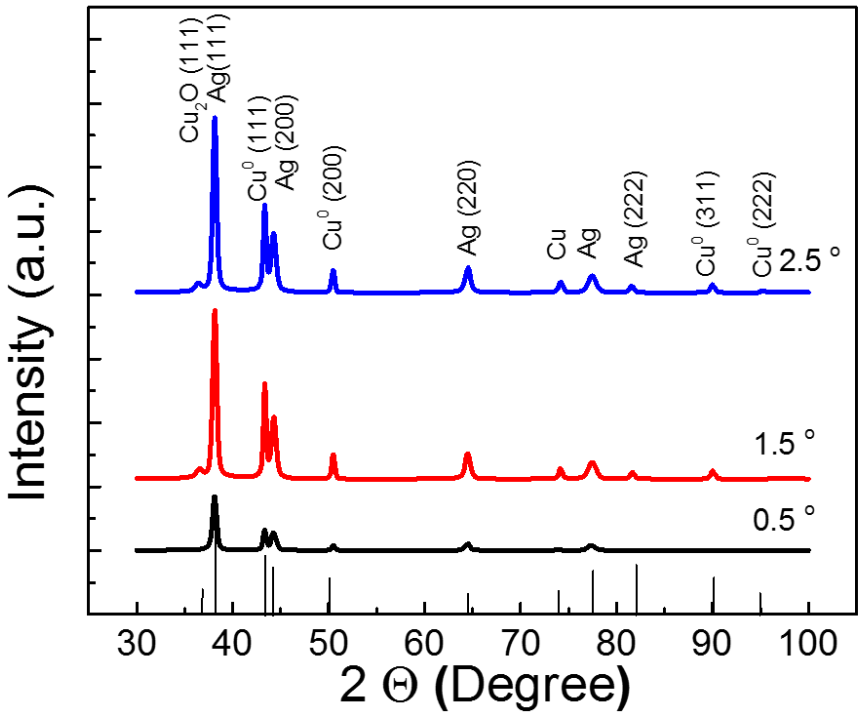

Figure S3. XRD pattern of CuAg nanocoral cathode at different fixed incident angles.

Table S1. XPS surface composition of CuAg nanocoral cathode

Elements / component peak	Binding energy (eV)	Chemical states	Surface conc. (at.%)
Cu 2p	932.4	Cu(I) (Cu_2O)	23.1
Cu 2p	934.6	Cu(II) (CuO; $Cu(OH)_2$; $CuCO_3$	3.5
O 1s	529.1	Cu(II)O (CuO)	0.5
	530.4	Cu(I)O (Cu_2O)	14.5
	531.5	CO_3^{2-}, OH^-	24.2
	532.7	C-O	3.1
Ag 3d	368.3	Ag(0)	1.0
C 1s	284.5	CH	19.1
	286.1	C-O	5.6
	288.8	CO_3^{2-}	5.4

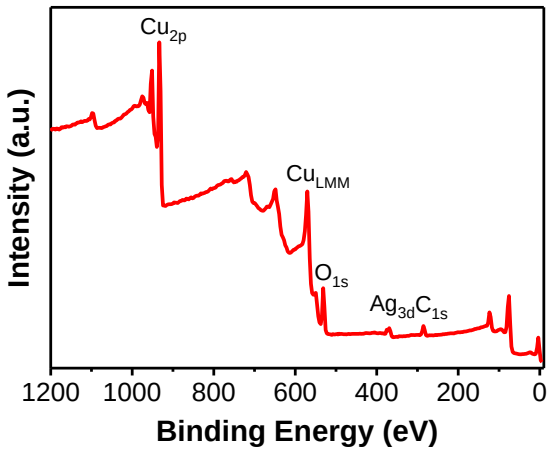

Figure S4. XPS survey scan of CuAg nanocoral cathode

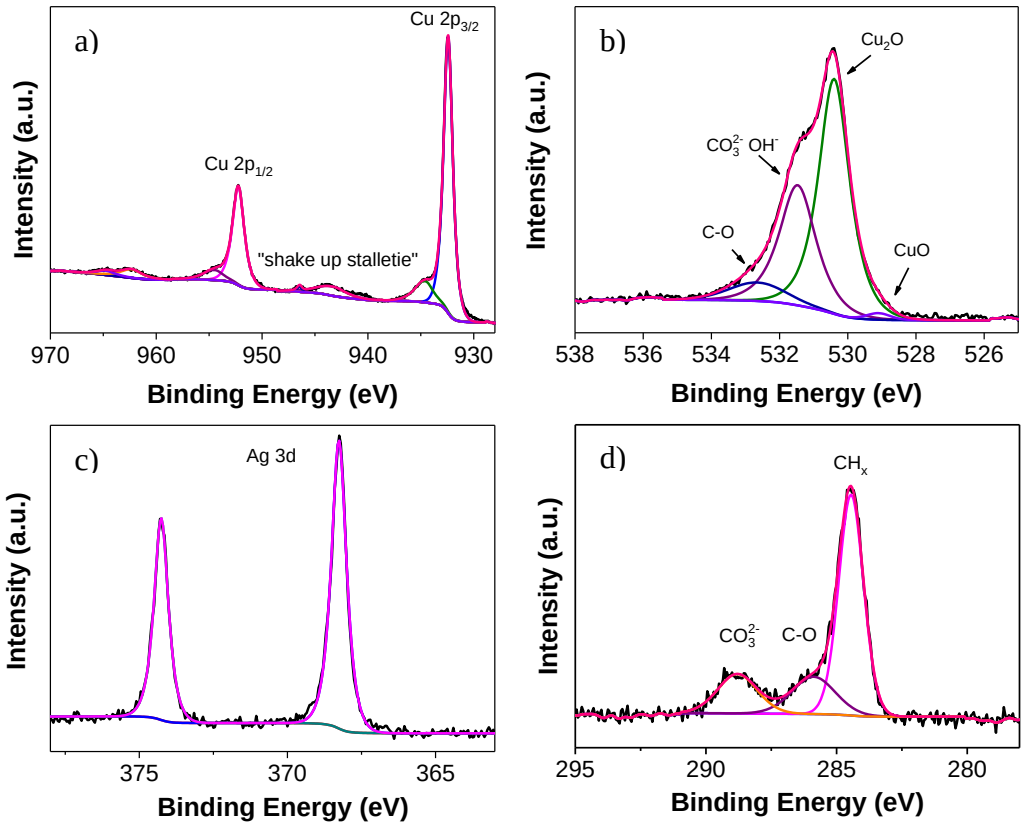

Figure S5. High-resolution XP spectra of the characteristic peaks: (a) Cu 2p; (b) O 1s; (c) Ag 3d; (d) C 1s.

Inductively coupled plasma mass spectroscopy (ICP-MS) analysis of CuAg cathode

We employed ICP-MS analysis of the catalytically active "nanocoral" region of the electrocathode, keeping in mind that this region was formed on top of a bulk Ag metal substrate. We mechanically removed portions of the "nanocoral" and performed the elemental analysis, acknowledging that the Ag content might be overestimated if the substrate is sampled. ICP-MS was performed using an Agilent 7900 system run using the He mode. The internal standard was Ge and Rh, selected based on their first ionization potentials and M/Z as compared to Cu and Ag respectively. Samples were digested with 1 mL of 70% HNO_3 (>99.999% trace metals basis, 225711, Sigma-Aldrich) and further diluted into 5 mL in total with 1% HNO_3 solution as the original sample solutions. An analysis of a number of samples so obtained finds that Ag is ca. 20-30% of the total metal concentration.

In-situ Raman spectroscopy measurements

As a qualitative guide, in-situ Raman spectroscopy was used to see the changes in the composition of the CuAg cathode. Raman measurements were performed in an electrochemical cell containing CuAg cathode, platinum anode, Ag/AgCl reference electrode and 0.1 M $KHCO_3$ with and without applied voltage. The Cu_2O peaks can be observed in Raman spectra of CuAg cathode before applying any potential but once we applied a slightly negative potential -0.6 V vs RHE on CuAg cathode all the Cu_2O peaks disappear (see figure below). This analysis clearly indicates that the oxygen content in CuAg cathode might be from atmospheric oxygen. Finally, we conclude that the subsurface O is probably similar to that of Cu catalysts made by similar electrochemical depositions.[17]

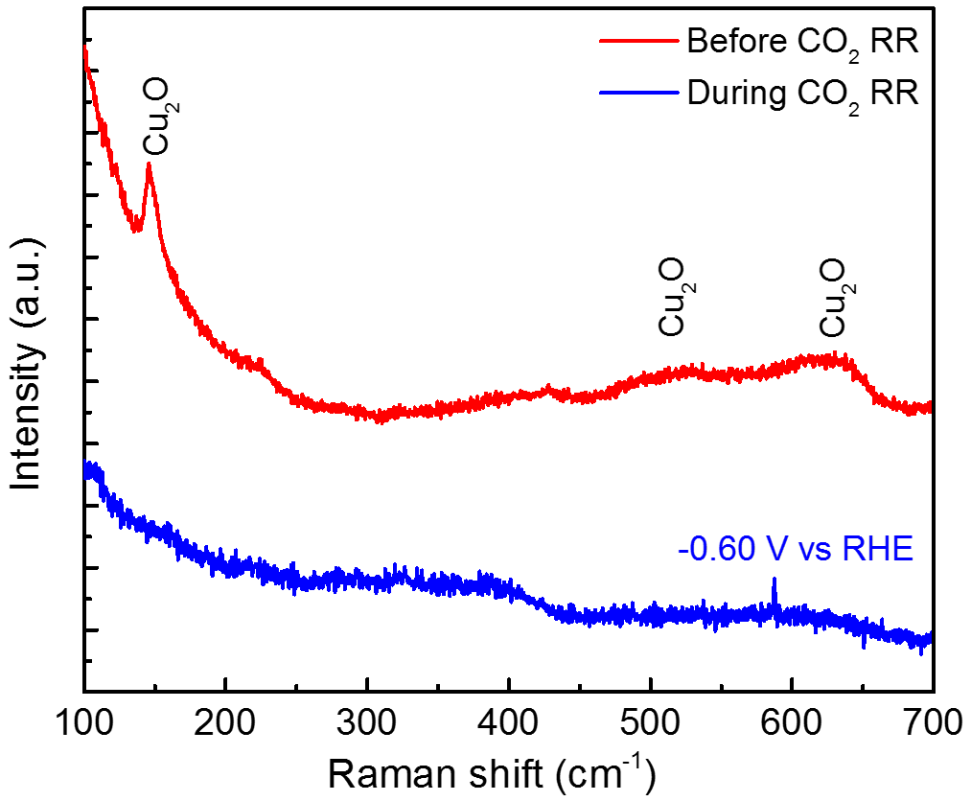

Figure S6. In-situ Raman spectra of CuAg cathode with and without applied voltage.

HRTEM analysis of CuAg cathode

We performed TEM, HRTEM measurements and corresponding HAADF-STEM-EDS mapping of CuAg cathode. These measurements were acquired on the TitanX microscope, located within the Molecular Foundry at Lawrence Berkeley National Labs. All data were acquired with an accelerating voltage of 200 keV. We have prepared the TEM sample by scratching the CuAg cathode with a copper metal tip. This scratched material was dispersed in isopropanol and ultrasonicated for 5 min. Finally, this solution is dropped on TEM grid (Si_3N_4) and air-dried. The TEM images and their corresponding EDS pattern shows distribution of Cu and silver (Figure S7). However, the active sites of sample might be damaged due to the sample preparation technique. The HRTEM images do not show the lattice spacing of Cu and Ag in CuAg cathode because the sample was too thick. Although we have calculated the lattice spacing (d_{Cu} = 2 Å and d_{Ag} = 2.3 Å) from Fourier transform (FFT). The HADDF-EDX pattern shows a distribution of copper and silver in CuAg cathode. The EDX mapping shows small particles of silver (green color) around Cu nanocoral (red color).

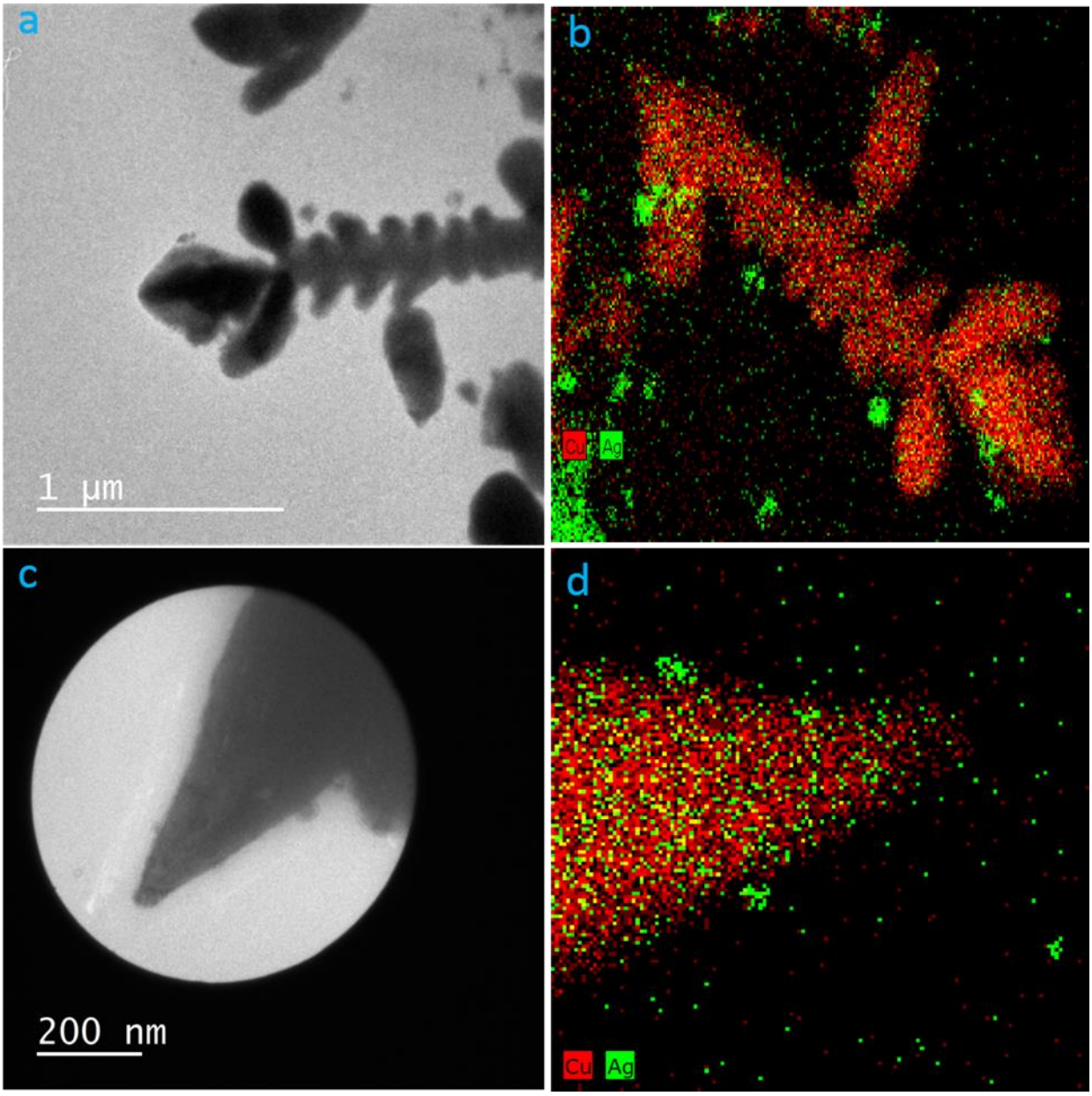

Figure S7. (a, c). TEM images of CuAg cathode, and (b, d). EDX images of the CuAg cathode.

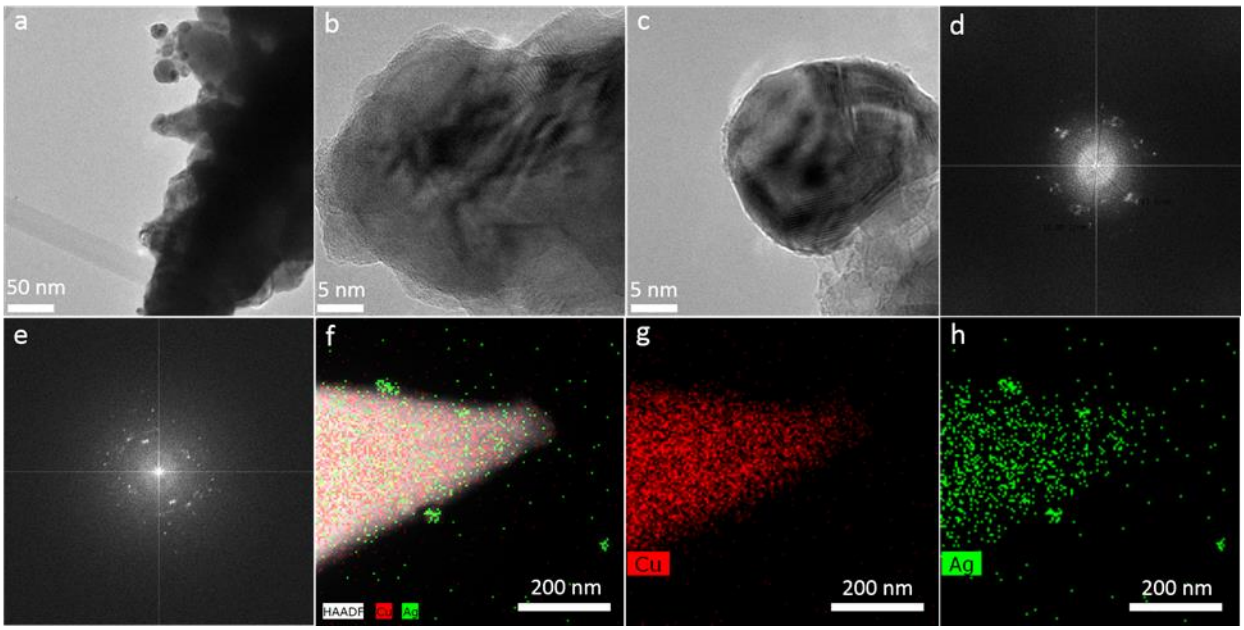

Figure S8. (a) TEM image of CuAg cathode, (b) HRTEM images of CuAg cathode, (c) HRTEM image of Ag nanoparticle on CuAg cathode, (d) FFT of CuAg cathode, (e) FFT of CuAg cathode from different area, (f) HAADF-EDX image of CuAg cathode, (g) Cu distribution in EDX pattern of CuAg cathode, and (h) Ag distribution in EDX pattern of CuAg cathode.

XRD and EDX analysis of IrO_2 anode

XRD data for the IrO_2 anode is shown in Fig. S5. An EDX line scan along the IrO_2 nanotube shows a uniform distribution of iridium, and there is no evidence of residual Zn from the ZnO template (Figure S6).

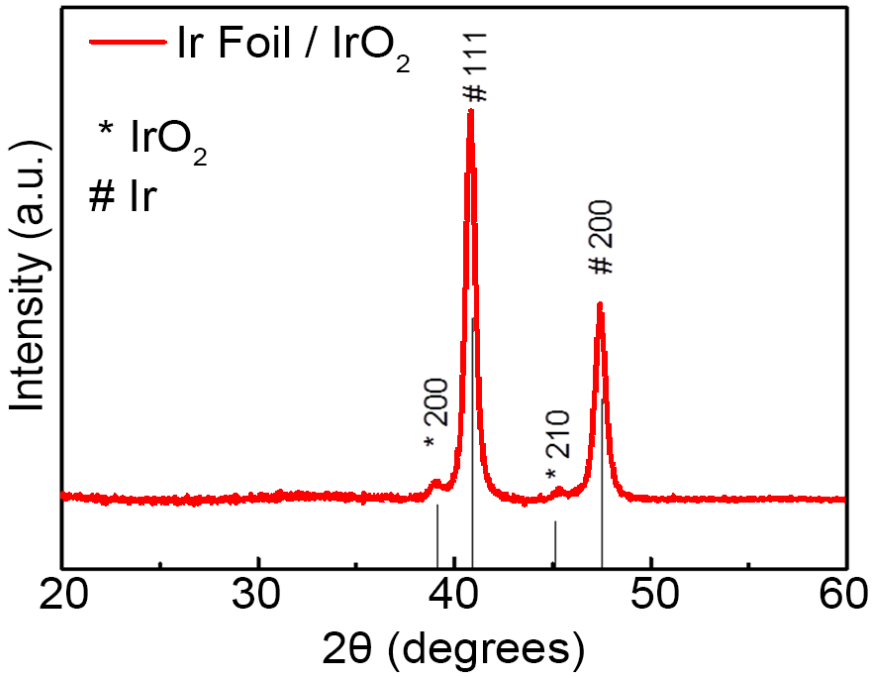

Figure S9. XRD pattern of IrO_2/Ir foil sample can be indexed to the characteristic diffraction peaks of Ir (JCPDS no. 03-065-1686), and IrO_2 (JCPDS no. 04-009-8479)

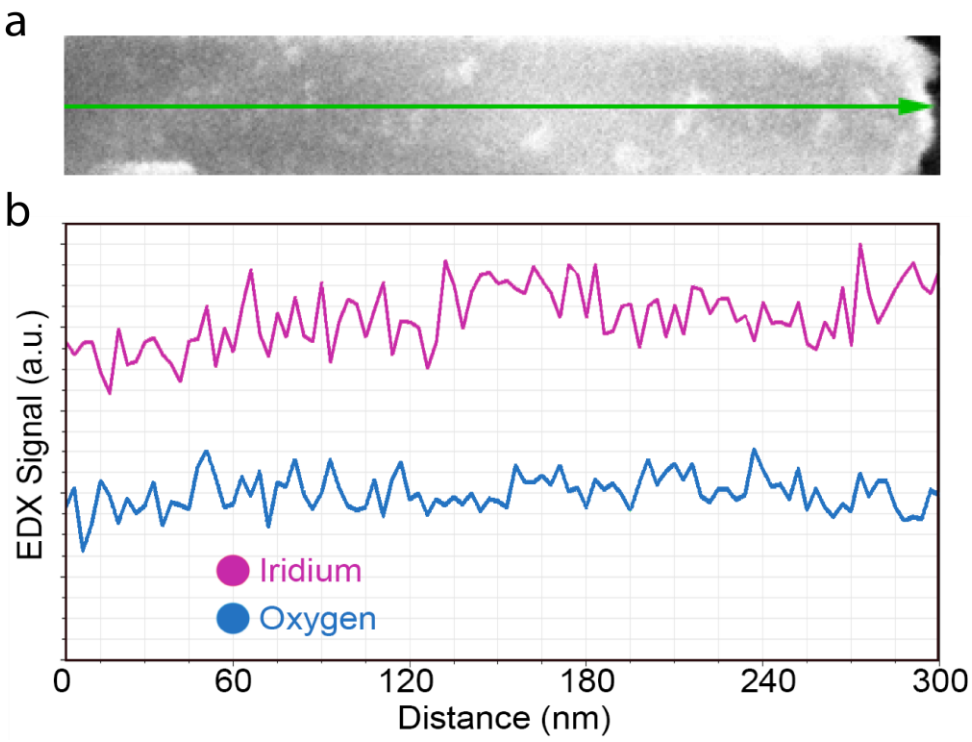

Figure S10. **a,** EDX elemental mapping of IrO_2 nanotubes on Ir foil. **b,** EDX line scan of IrO_2 nanotubes on Ir foil.

CuAg nanocoral cathode stability

We performed longer term (three days) measurements of CuAg cathode in three electrode configuration and in 0.1 M $CsHCO_3$ at 1 V vs RHE to fully understand the stability of the catalyst. A small decrease (nearly 15% after 24 hrs) in the current density of the catalyst was observed, which may be due to contamination. Consequently, we changed the electrolyte after every 24 hrs and the CuAg cathode regain the performance (see the J-V curve below). An increase in CO Faradaic efficiency was also observed with time, whereas the Faradaic efficiency of hydrogen and ethylene slightly decrease, which again indicate the contamination. The Faradaic efficiency of most C_2-C_3 products were constant during the course of time. Finally, the CuAg nanocoral cathode shows excellent stability. This is the extra ordinary performance of our CuAg catalyst.

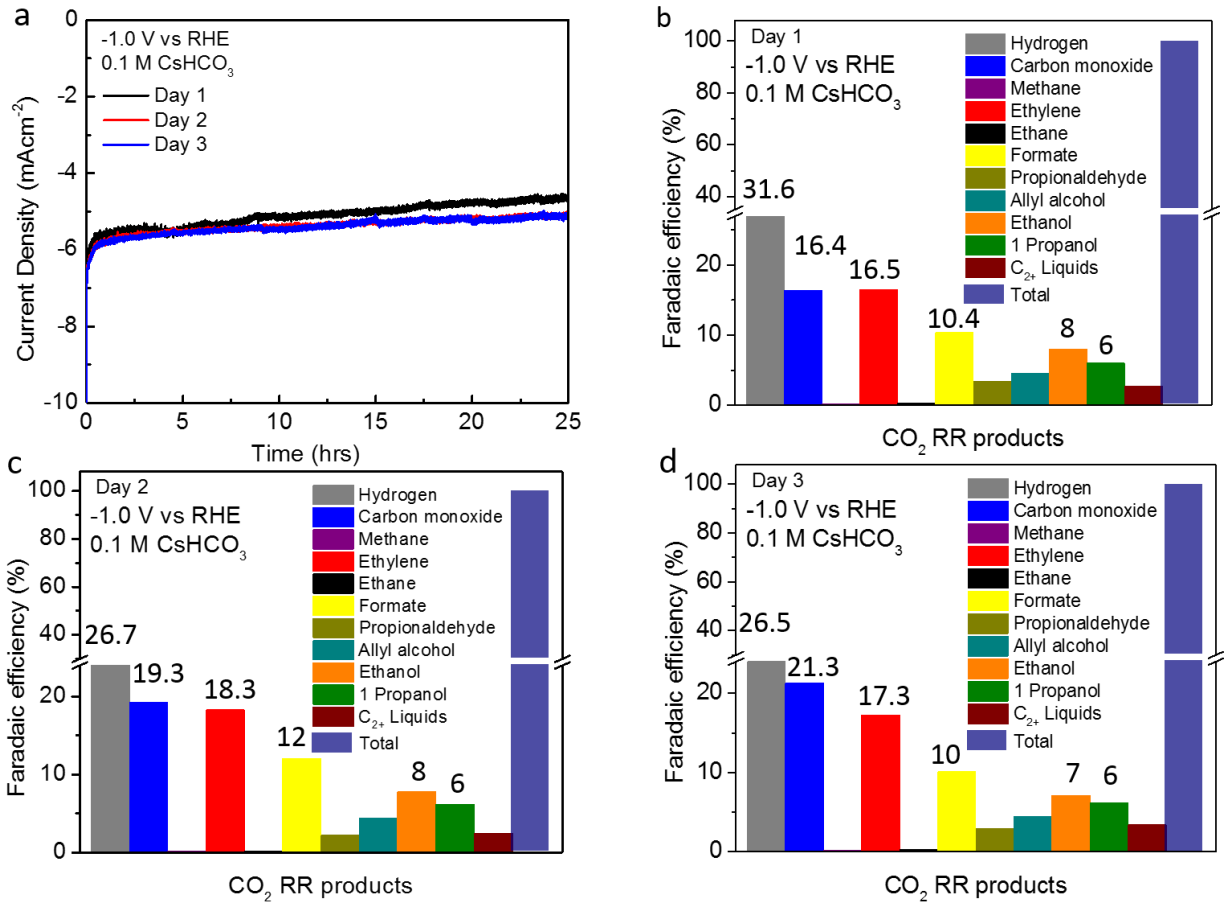

Figure S11. (a) Current density data of CuAg photocathode for three days., (b-d) Faradaic efficiency data of CuAg cathode at 1 V vs RHE in 0.1 M $CsHCO_3$ of day 1-3.

IrO_2 stability Measurements

We operated IrO_2/Ir foil anode in 0.2 M $CsHCO_3$ at 1.6 V vs RHE for three days and found excellent stability. A current drop was observed in Ir/IrO_2 anode performance after 20 hrs as a result of bubble accumulation on the surface. After mechanical agitation of the electrode for few minutes to remove the bubbles, the original performance is restored (Fig. S2).

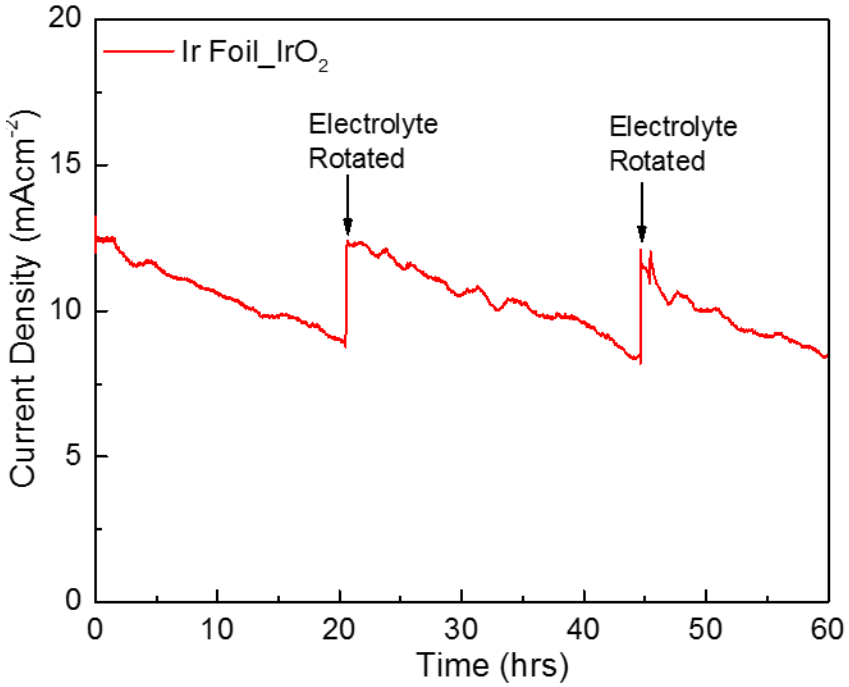

Figure S12. Stability measurement of Ir-IrO_2 anode at 1.6 V vs RHE in 0.2M $CsHCO_3$.

Supplemental electrochemical data

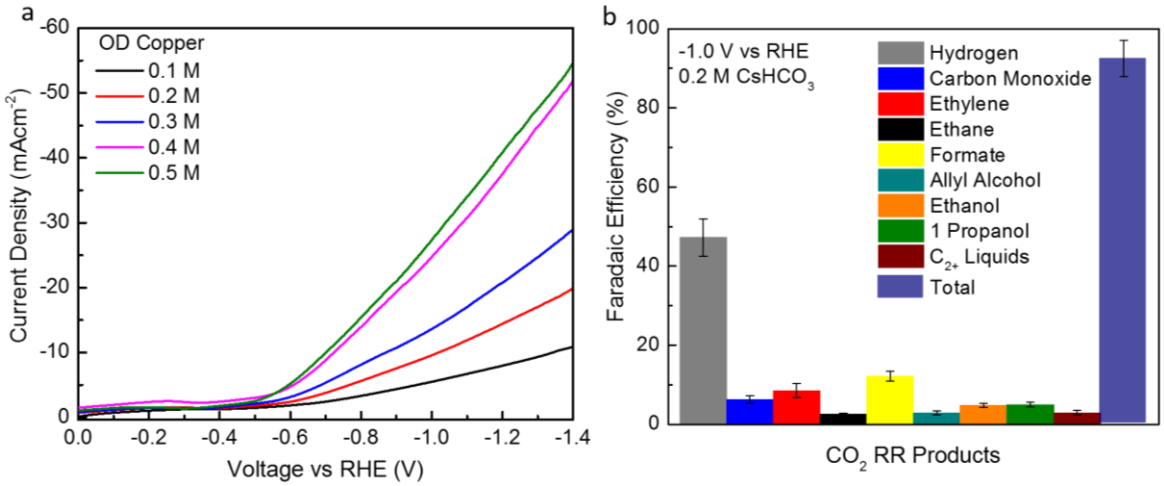

Figure S13. Three-electrode measurements performed with an oxide-derived (OD) copper cathode. **a,** Measured current density with voltage vs RHE in different (0.1-0.5 M) $CsHCO_3$ electrolytes. **b,** CO_2 RR products at -1 V vs RHE in 0.2 M $CsHCO_3$. An Ag/AgCl reference electrode and an IrO_2 nanotube anode were used and the cell was sparged with CO_2 bubbling at a rate of 5 sccm.

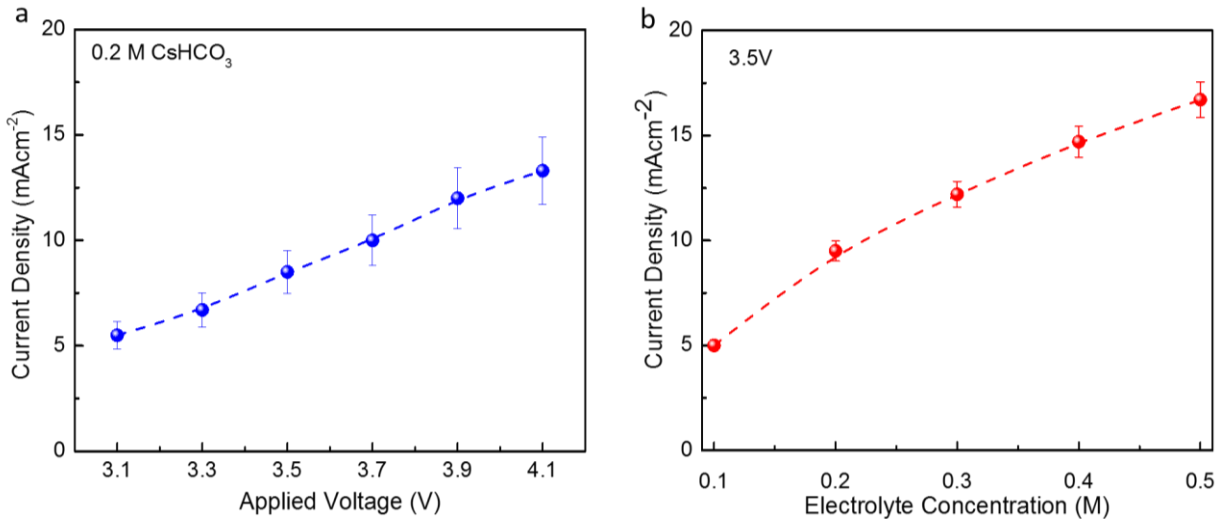

Figure S14. CO_2 reduction performed in two-electrode configuration with CuAg nanocoral cathode and IrO_2 nanotubes anode under constant CO_2 bubbling at a rate of 5 sccm. **a,** Measured current density with applied bias in 0.2 M $CsHCO_3$ electrolyte during CO_2 RR. **b,** Measured current density with different concentrations at 3.5 V.

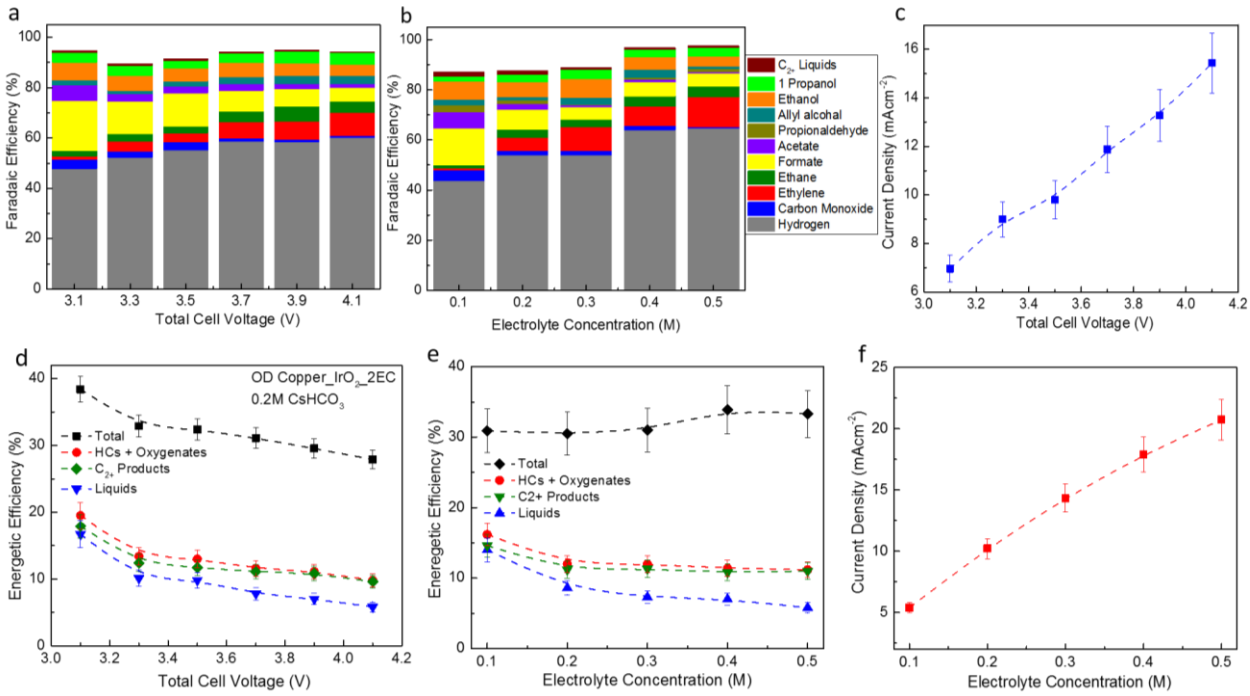

Figure S15. Two electrode measurements of oxide derived (OD) copper cathode and IrO_2 nanotube anode under constant CO_2 bubbling at a rate of 5 sccm. **a,** CO_2 RR products as a function of applied voltage in 0.2 M $CsHCO_3$. **b,** CO_2RR products with different electrolyte concentration (0.1-0.5 M) at a fixed applied voltage of 3.5 V. **c,** Measured current density with applied bias during CO_2 RR. **d,** Energetic efficiency (overall electrolyzer conversion efficiency) with applied bias. **e,** Energetic efficiency as a function of electrolyte concentration. **f,** Measured current density with electrolyte concentration.

Optimization of CO_2 electrolysis cell

We tested electrochemical CO_2 reduction reaction in different electrolyte concentrations (0.1-0.5 M) of $CsHCO_3$. The current increases with electrolyte concentration at all potentials; however, an optimization of suitable current at all electrolyte concentrations is necessary to obtained desired hydrocarbons and oxygenates. The CO_2 could be depleted at the surface of electrode, if we run the electrochemical cell at high current density ($\geq$25 mA cm^{-2}). We chose a potential (2.5-4.1 V) and electrolyte concentration (0.1-0.5 M $CsHCO_3$) window, with the goal of keeping the current density less than 20 mA cm^{-2}. An increase in the hydrogen Faradaic efficiency was observed after increasing the electrolyte concentration beyond 0.5 and at voltages over 4.1 V in 0.5 M $CsHCO_3$, this might be due to CO_2 depletion at the electrode surface. However, we found 0.5 M $CsHCO_3$ electrolyte concentration superior in comparison of lower concentrations because this provides higher current density and excellent selectivity for hydrocarbons and oxygenates at all illumination

conditions. These high operating current density values provides high solar to fuel conversion efficiency.

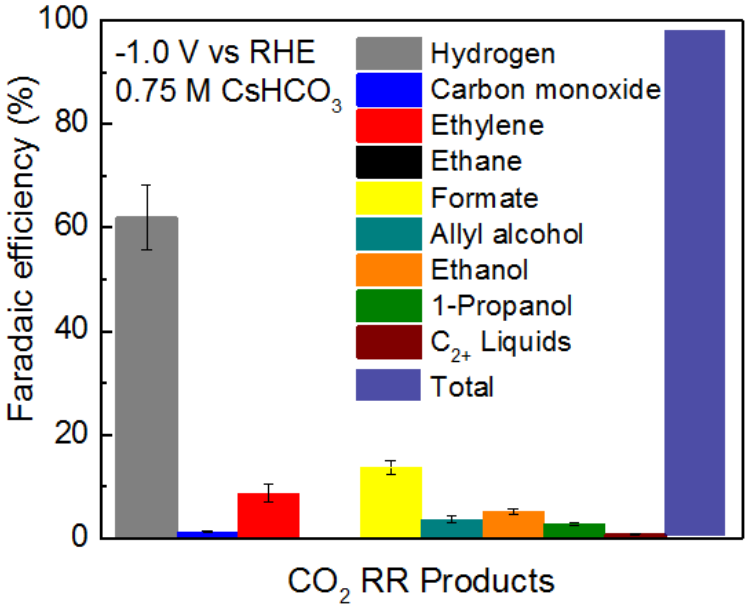

Figure S16. CO_2 RR products distribution of CuAg cathode at -1 V vs RHE in 0.75 M $CsHCO_3$ electrolyte.

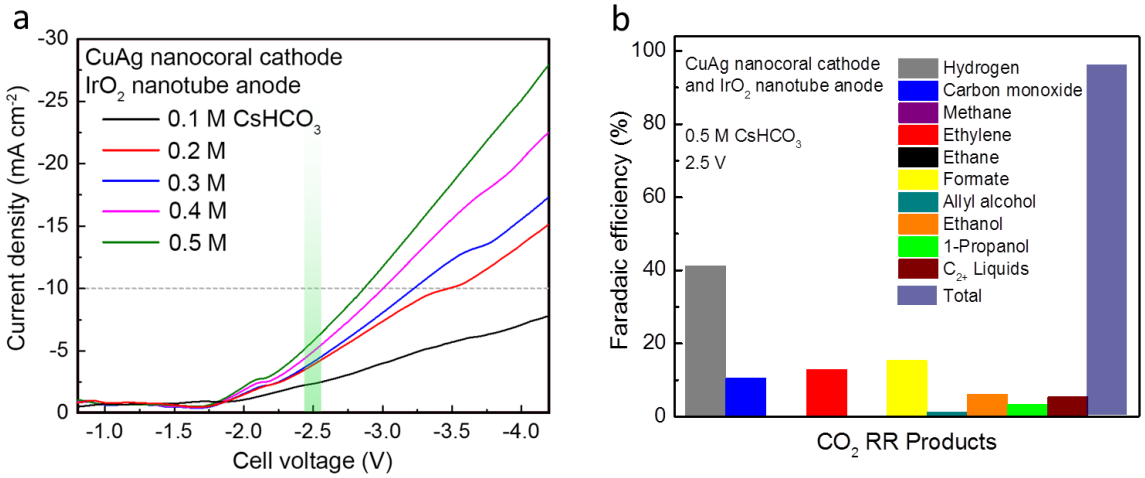

Figure S17. **a,** Linear scan voltammetry curve of a CuAg nanocoral cathode in a two-electrode configuration with an IrO_2 nanotube anode in different electrolyte concentrations (0.1-0.5 M $CsHCO_3$)

during CO_2 RR. The green bar marks the operating voltage when using a 0.5 M electrolyte concentration. **b,** CO_2 RR products distribution at 2.5 V in 0.5 M $CsHCO_3$ electrolyte.

Table S7. CO_2 RR products observed in this study.

CO_2 RR Products				
Total	**HCs+Oxygenates**	**C_{2+} Products**	**Liquids**	**C_{2+} Liquids**
Hydrogen	Methane	Ethylene	Formate	Acetate
Carbon Monoxide	Ethylene	Ethane	Acetate	Acetaldehyde
Methane	Ethane	Acetate	Acetaldehyde	Propionaldehyde
Ethylene	Formate	Acetaldehyde	Propionaldehyde	Allyl Alcohol
Ethane	Acetate	Propionaldehyde	Allyl Alcohol	Ethanol
Formate	Acetaldehyde	Allyl Alcohol	Ethanol	Propanol
Acetate	Propionaldehyde	Ethanol	Propanol	Hydroxyacetone
Acetaldehyde	Allyl Alcohol	Propanol	Hydroxyacetone	Ethylene Glycol
Propionaldehyde	Ethanol	Hydroxyacetone	Ethylene Glycol	Glyoxal
Allyl Alcohol	Propanol	Ethylene Glycol	Glyoxal	Glycolaldehyde
Ethanol	Hydroxyacetone	Glyoxal	Glycolaldehyde	
Propanol	Ethylene Glycol	Glycolaldehyde		
Hydroxyacetone	Glyoxal			
Ethylene Glycol	Glycolaldehyde			
Glyoxal				
Glycolaldehyde				

Supplemental solar-driven CO_2 data

I. Two series-connected silicon solar cells connected in series with an MPP Tracker and an electrochemical cell

Two commercial silicon solar cells were connected to a maximum power point (MPP) tracker and an electrochemical cell for CO_2 reduction (Fig S10). A total illumination area of 3.198 cm^2 was used. Different optical density filters (ND-0.1, ND-0.3, ND-0.5) were used to control the illumination intensity (0.83-sun, 0.53-sun, and 0.35-sun, respectively). These cells provide different currents (60.9 mA, 53.3 mA, 34.2 mA, and 22.8 mA) under different illumination conditions (1.0-sun, 0.83-sun, 0.53-sun and 0.35-sun, respectively).

After coupling these solar cells with the MPP tracker/boost converter, we measured the input (from solar cells to MPP) and output (from MPP to Electrochemical cell) current/voltage by connecting a multi-meter in series and parallel (Table S8). Both the input and output voltages depend on the load (electrochemical cell), which is non-linear and different for for each electrolyte concentration. We chose a value for the MPP feedback resistor to limit the output to 3.6 V. With this configuration, the output of the circuit was between 2.5 and 3.6 volts over the range of electrolyte concentration (0.1-0.5 M) and illumination (0.35 to 1-suns) employed, as shown in Table S8.

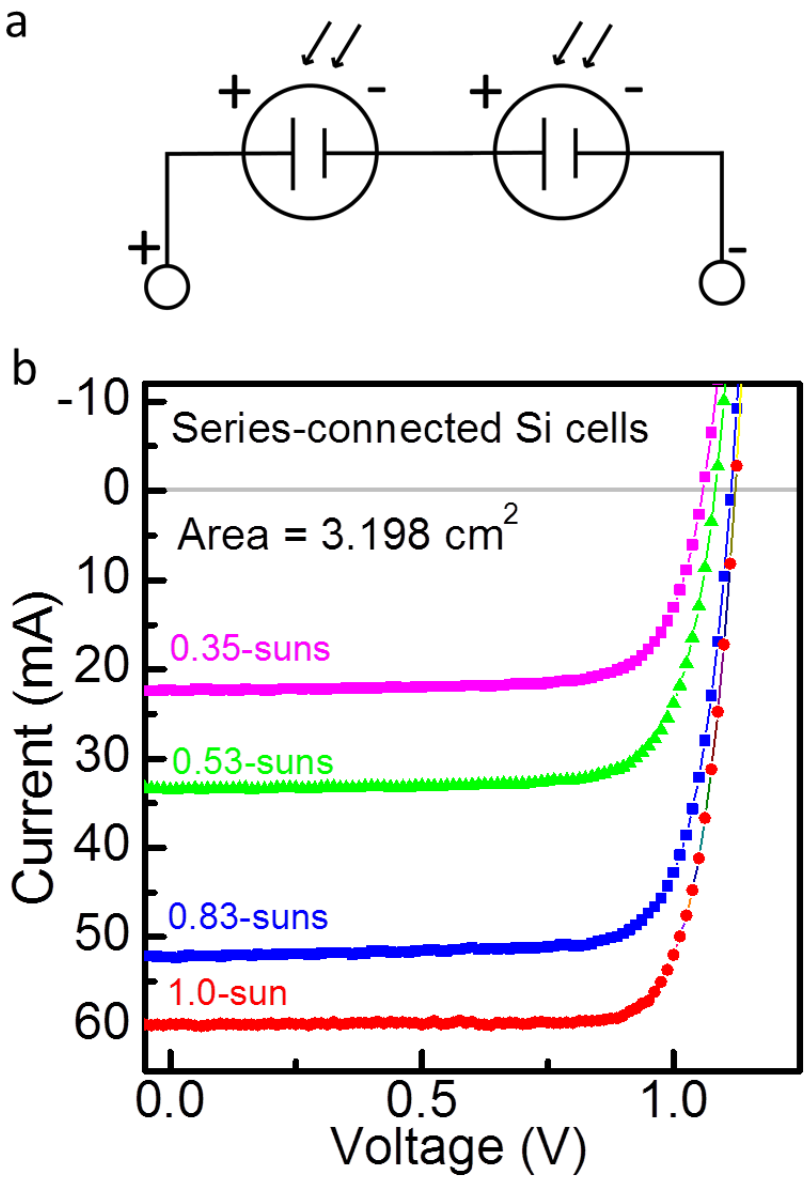

Figure S18. **a,** Circuit diagram of series-connected Si solar cells. **b,** I-V curves of the two series-connected silicon solar cells depicted schematically in **a** at different illumination conditions (0.35 to 1-sun) with an illumination area of 3.198 cm^2.

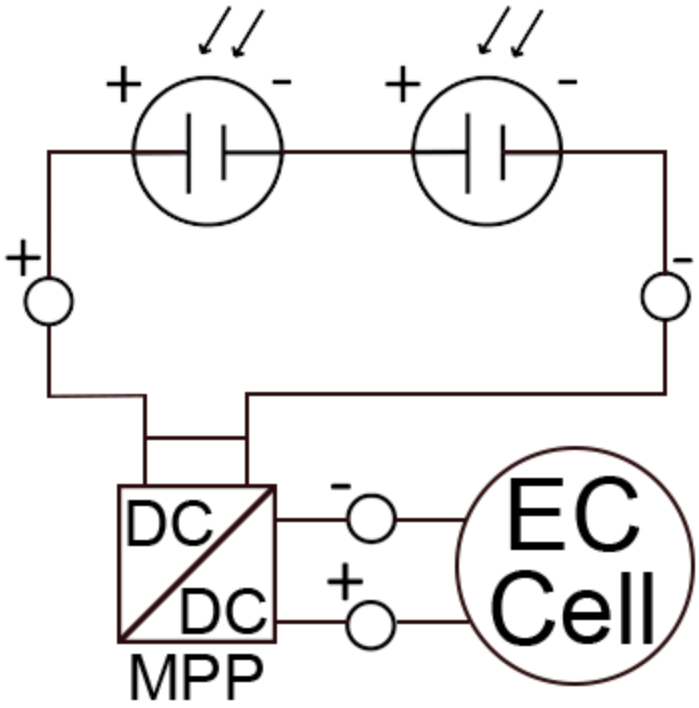

Figure S19. TD1 circuit diagram.

Table S8. I-V data of TD1 in different electrolyte concentrations (0.1-0.5 M $CsHCO_3$) and various illumination conditions (0.35 to 1-sun); EC = Electrochemical cell.

	Electrolyte Concentration (M)	V_{mp} (MPP input)	I_{mp} (MPP input)	V_{cell} (EC input)	I_{cell} (EC input)	η_{MPP} (%)
1.0-sun	0.1	1.07	30.40	3.59	6.36	70
	0.2	1.02	48.70	3.59	9.9	95
	0.3	0.907	56.00	3.39	13.76	92
	0.4	0.904	55.40	3.21	14.62	92
	0.5	0.912	55.9	3.13	15.11	93
0.83-sun	0.1	1.06	30.06	3.59	6.01	72
	0.2	0.967	48.6	3.59	9.62	75
	0.3	0.878	51.6	3.16	11.61	85
	0.4	0.876	47.9	3.11	11.91	89
	0.5	0.878	45.7	2.91	12.70	92
0.53-sun	0.1	0.981	30.35	3.59	5.96	72
	0.2	0.846	35.31	3.32	7.70	86
	0.3	0.850	36.34	3.04	8.93	85
	0.4	0.850	31.63	2.78	9.01	93
	0.5	0.853	32.40	2.67	9.42	91
0.35-sun	0.1	0.838	23.56	3.44	4.95	86
	0.2	0.841	24.82	3.09	5.78	86
	0.3	0.834	22.37	2.66	6.42	92
	0.4	0.835	21.10	2.57	6.50	95
	0.5	0.840	23.21	2.48	6.67	92

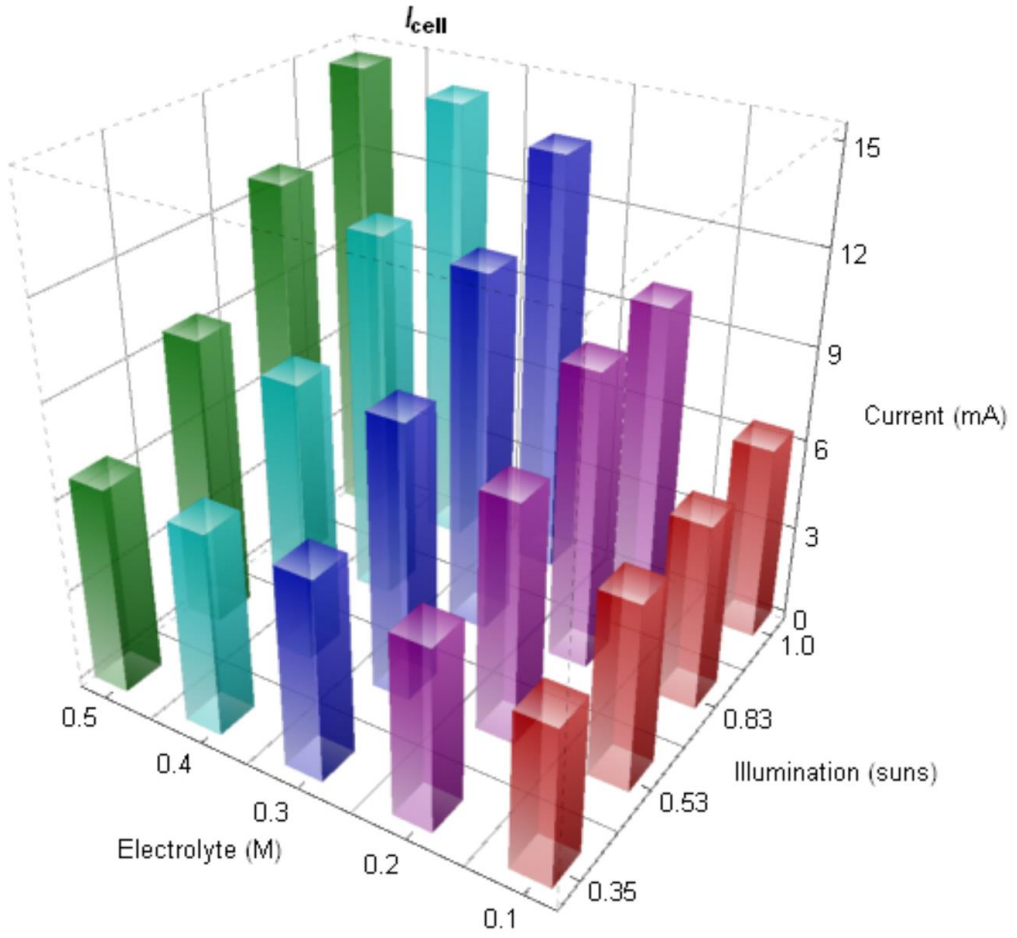

Figure S20. TD1 Cell current as a function of electrolyte concentration and illumination intensity.

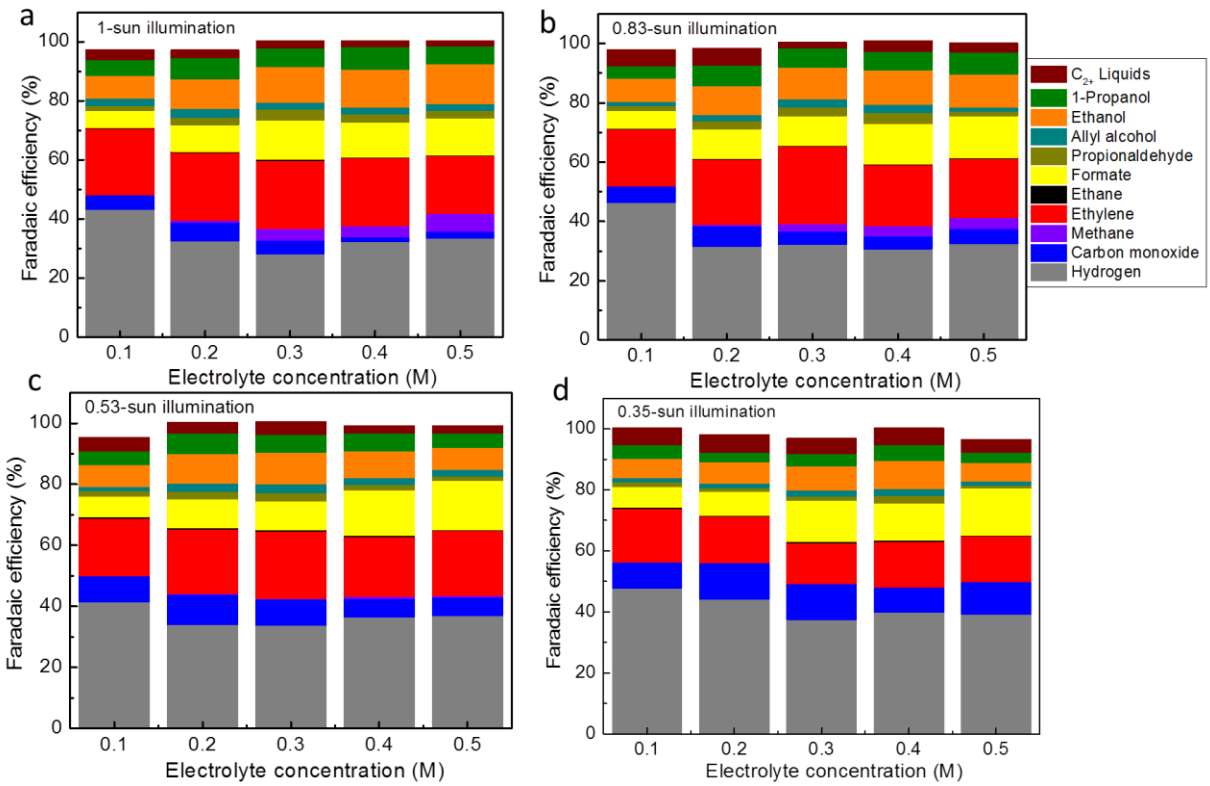

Figure S21. Faradaic efficiency of CO_2 RR products under various illumination conditions. **a,** 1.0-sun. **b,** 0.83-sun. **c,** 0.53-sun. **d,** 0.35-sun.

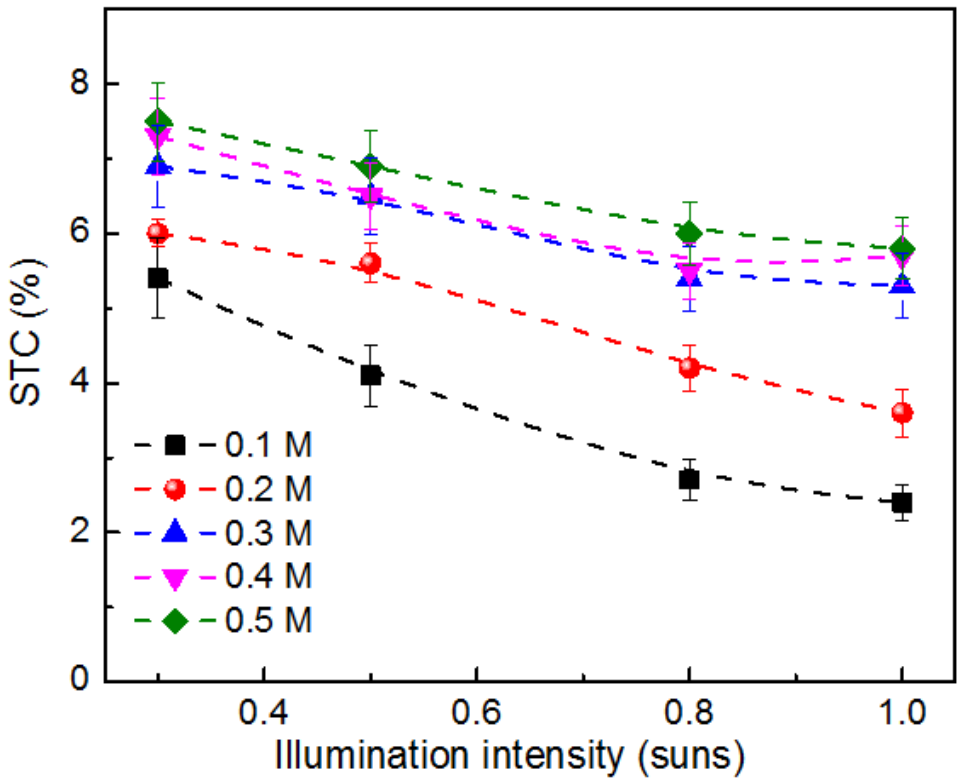

Figure S22. Total solar-to-chemical conversion efficiency to CO_2 RR products of TD1 under various illumination conditions and electrolyte concentrations.

Table S9. Efficiency results for TD1.

Solar to All Products (%)	0.1 M $CsHCO_3$	0.2 M $CsHCO_3$	0.3 M $CsHCO_3$	0.4 M $CsHCO_3$	0.5 M $CsHCO_3$
Cell efficiency (%)	35.8	41.6	45.5	48.7	50.3
1.0-sun	2.4	3.6	5.3	5.7	5.8
0.83-sun	2.7	4.2	5.4	5.5	6.0
0.53-sun	4.1	5.6	6.5	6.5	6.9
0.35-sun	5.4	6.0	6.9	7.3	7.5
Solar to hydrocarbons and oxygenates (%)					
1.0-sun	1.2	2.1	3.6	3.7	3.8
0.83-sun	1.3	2.5	3.3	3.6	3.6
0.53-sun	1.9	3.1	3.7	3.7	3.9
0.35-sun	2.3	2.4	3.4	3.7	3.8

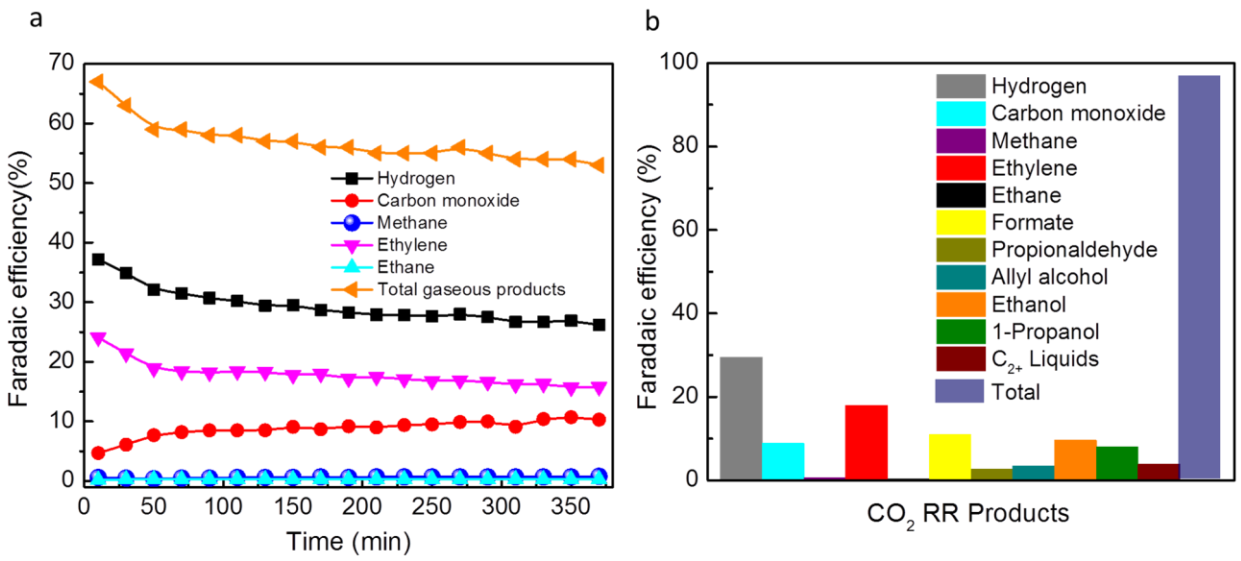

Figure S23. TD1 stability. 6-hour CO_2RR test in 0.2 M $CsHCO_3$, Cell efficiency 33%, Solar to all products 3.2%, solar to hydrocarbons and oxygenates, 2.0%. **a,** Faradaic efficiency data for gaseous products of TD1 for 6 hrs. **b,** Faradaic efficiency data for all products of TD1.

II. Four-Terminal III-V/Silicon tandem solar cell connected to two MPP trackers in parallel with electrochemical cell

Two III-V/silicon tandem solar cells were connected individually (top cells and bottom cells) to two MPP trackers (with each cell on its own tracking/boost board). These MPP/boost boards were connected in parallel to an electrochemical cell to provide constant voltage (Fig. S14). A total illumination area of 2.0 cm^2 was used in this study. We used two different MPP trackers to account for current mismatch between the two absorbers. We used 1-sun illumination with different concentrations (0.1-0.5 M) of the $CsHCO_3$ electrolyte. The current and voltage characteristics of this device can be seen in Table S10.

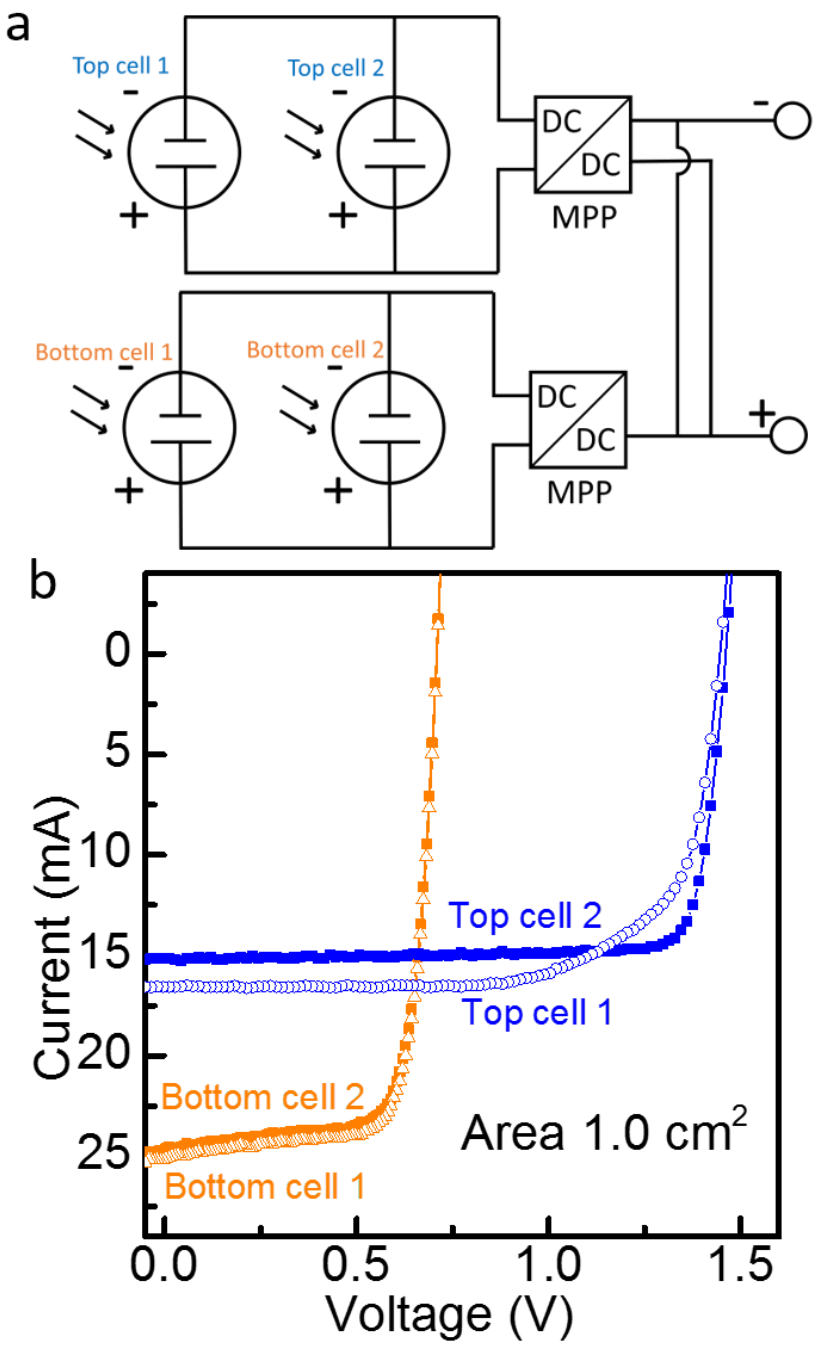

Figure S24. I-V curve of four-terminal Si/III-V tandem solar cell configuration at 1 Sun illumination with an illumination area of 2.0 cm^2.

Table S10. I-V data of TD2 at 1-sun illumination and different (0.1-0.5 M $CsHCO_3$) electrolyte concentrations; EC = Electrochemical cell.

Electrolyte Concentration (M)	V_{top} (MPP-1)	I_{top} (MPP-1)	V_{bottom} (MPP-2)	I_{bottom} (MPP-2)	V_{out} (EC input)	I_{out} (EC input)	η_{MPP} (%)
0.1	1.12	11.1	0.59	17.1	3.5	5.4	84
0.2	1.11	21.3	0.65	23.5	3.5	8.8	79
0.3	1.11	21.2	0.57	42.7	3.2	11.9	81
0.4	1.11	19.9	0.57	36.1	3.1	12.3	89
0.5	1.11	21.1	0.57	36.0	3.0	13.2	89

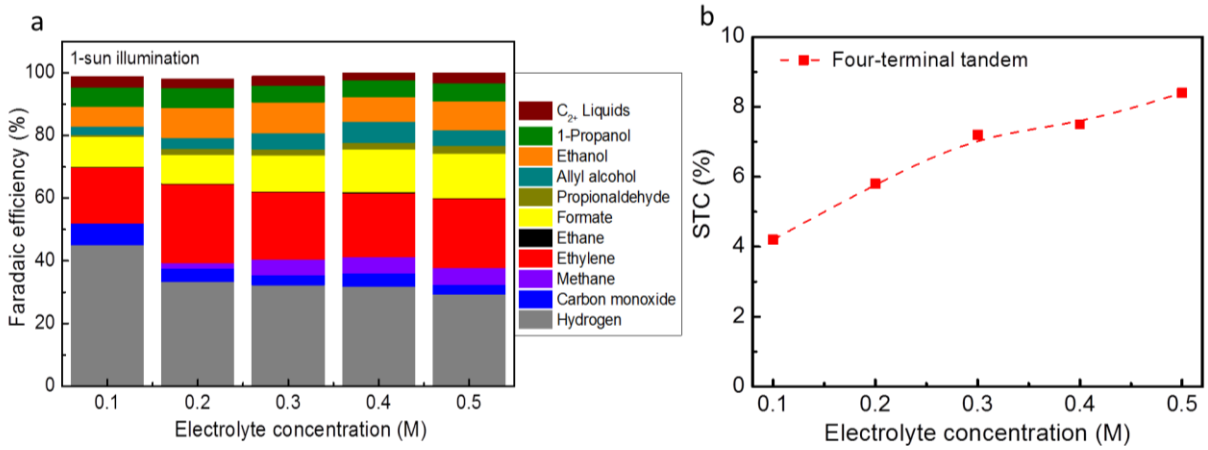

Figure S25. a, CO_2 RR products of TD2 under 1-sun illumination in different electrolyte concentrations (0.1-0.5M $CsHCO_3$). **b,** Total solar to fuel conversion efficiency of CO_2RR products in different electrolyte concentrations and under 1-sun illumination of TD2.

Table S11. Efficiency results of TD2

	0.1M $CsHCO_3$	0.2M $CsHCO_3$	0.3M $CsHCO_3$	0.4M $CsHCO_3$	0.5M $CsHCO_3$
Cell efficiency (%)	34.7	34.0	37.2	39.6	40.8
Solar to all products (%) at 1-sun	4.2	5.8	7.2	7.5	8.4
Solar to hydrocarbons (%) at 1-sun	**1.9**	**3.5**	**4.5**	**4.8**	**5.6**

SEM and XRD pattern of CuAg cathode before and after CO_2 RR

We have measured the SEM images and XRD patterns of the CuAg cathode and the IrO_2 anode after operation in the CO_2 reduction cell. CuAg cathode was operated in 0.1 M $CsHCO_3$ at 1 V vs RHE for 2 hrs and IrO_2 anode used as a counter electrode during this reaction. We do not observe any changes in surface morphology of CuAg cathode and IrO_2 anode. Although, a small change in XRD pattern of CuAg cathode can be seen afte CO_2 RR measurement, whereas there was no change observed in XRD pattern of IrO_2 after reaction. XRD pattern of CuAg shows an increase in the relative intensity of Ag after CO_2 RR, which indicates that there may be more silver on the surface. Some sample data is provided below.

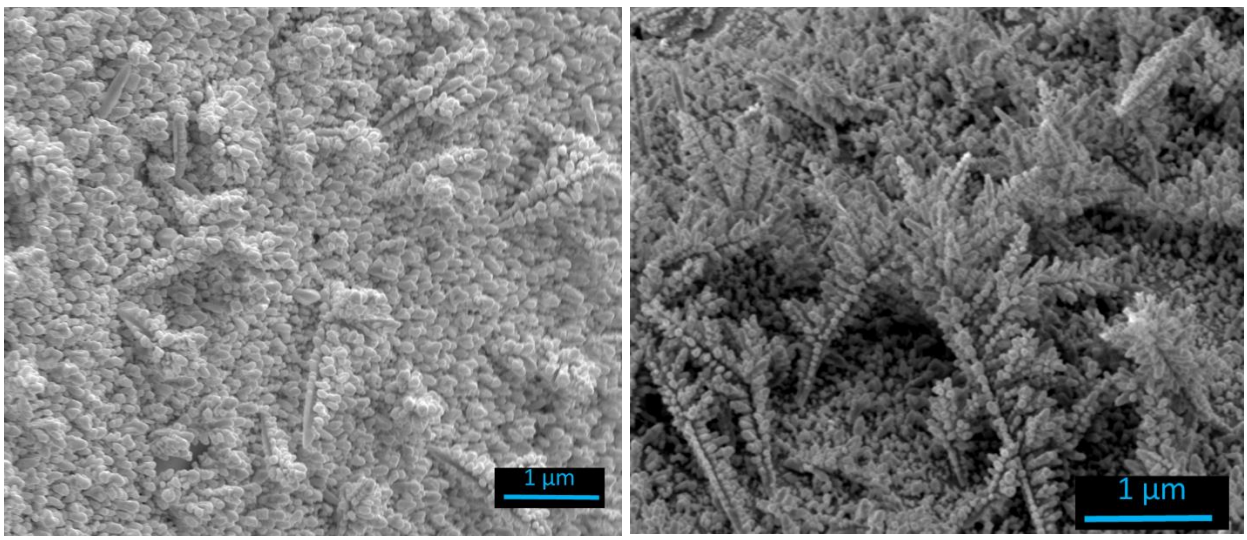

Figure S26. SEM surface view of CuAg cathode before (left) and after (right) CO2 RR in 0.1 M CsHCO3 at 1 V vs RHE for 2 hrs.

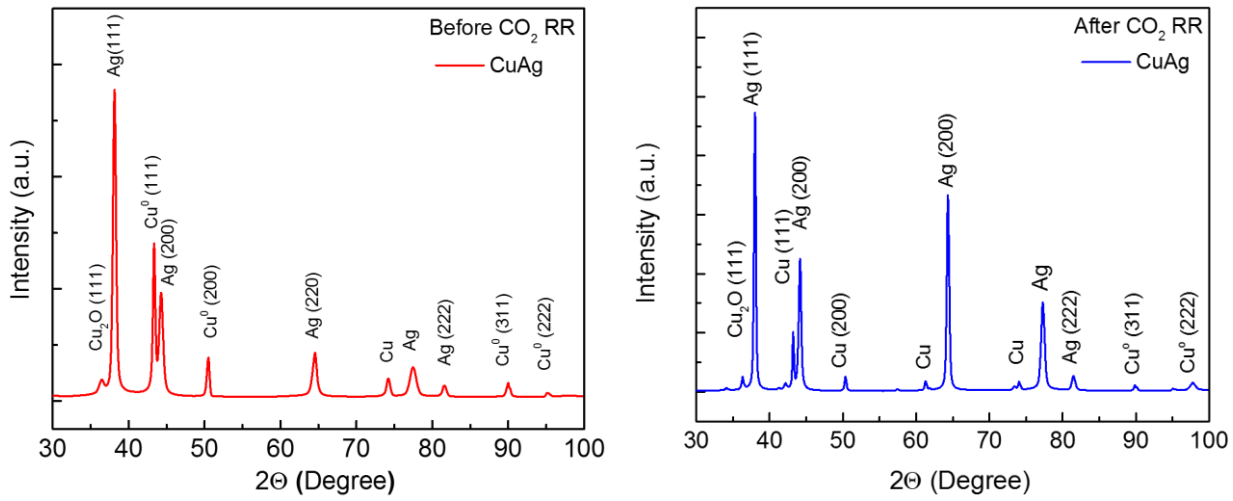

Figure S27. XRD pattern of CuAg cathode before (left) and after (right) CO_2 RR in 0.1 M $CsHCO_3$ at 1 V vs RHE for 2 hrs.

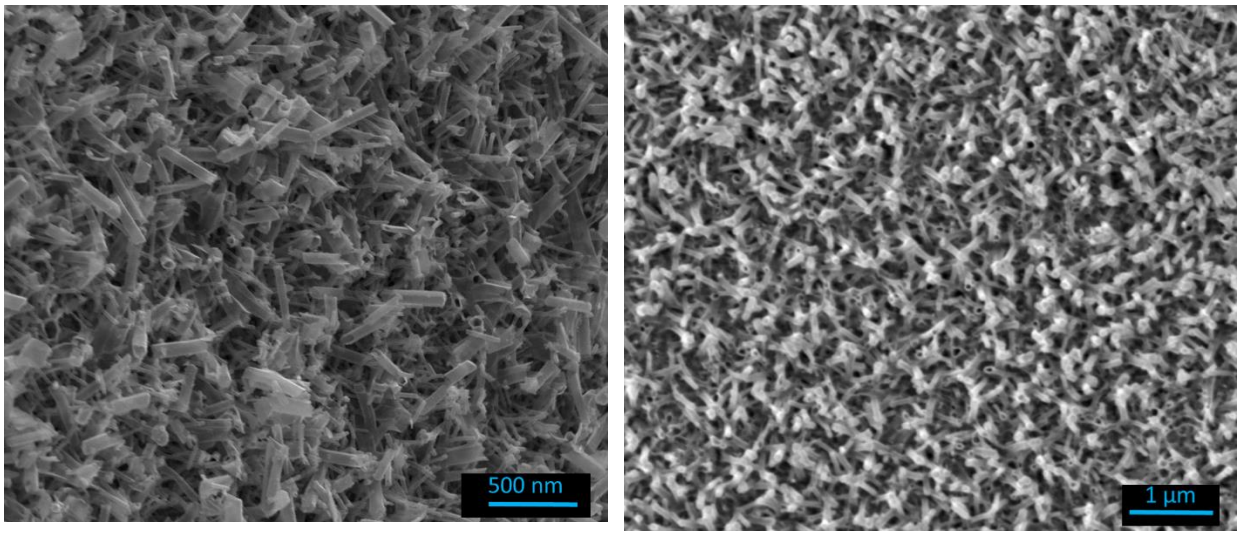

Figure S28. SEM surface morphology of IrO_2 nanotube anode before (left) and after (right) operation in 0.1 M $CsHCO_3$ for 2 hrs.

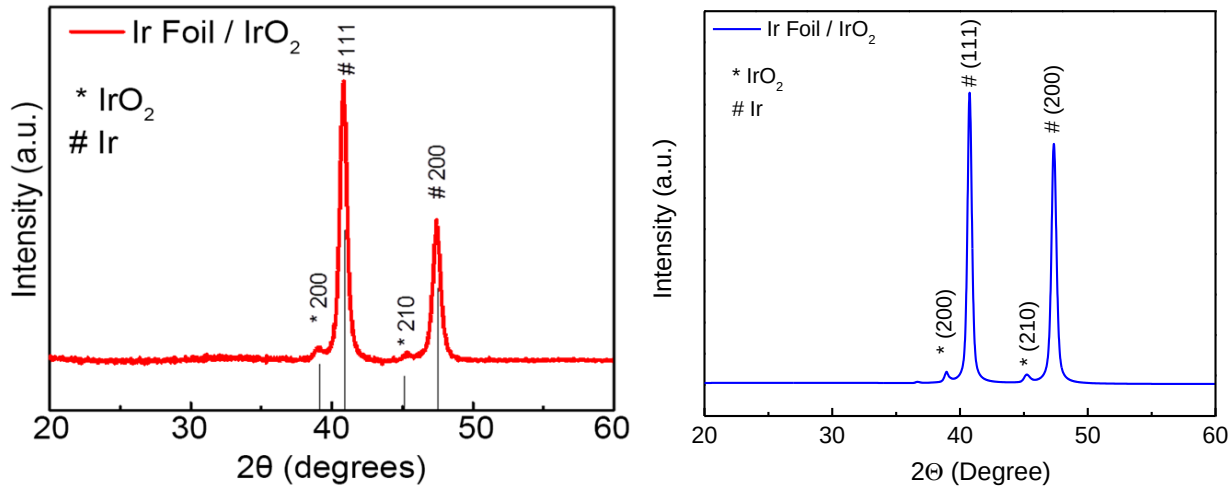

Figure S29. XRD pattern of IrO_2 anode before (left) and after (right) CO_2 RR in 0.1 M $CsHCO_3$ for 2 hrs.

Techno-economic analysis of solar-driven CO_2 reduction device

The technological readiness level (TRL) of our device is 3-4. While we have demonstrated the ability to produce chemical fuels, we have not demonstrated the separation of products, which remains a challenge for future work. Nevertheless, it is possible to construct a simple, prospective techno-economic analysis. The following simplifying assumptions are made:

- The CO_2 feedstock is provided to the system without cost, as a result of an incentive program (such as a carbon tax).
- The method will have been developed such that the carbon dioxide feedstock can be recycled.
- The system is coupled to a standard ca. 1 m^2 silicon solar module with a 200 W nameplate rating.
- The cost and method of product separation is not considered.
- As our long-term testing shows that electrolyte contamination is a concern, a method of filtering or otherwise maintaining the purity of the electrolyte will have to be implemented.

Based on the area ratio of the solar cell to the catalyst active area, which is 2:1, we will estimate the cost of an electrolysis cell that matches the commercially-available 1 m^2 solar cell

chosen. When scaling up this technology, we will not use iridium or silver foil as supports for the cathode and anode. If we assume the cathode is 1 μm thick, and is comprised of 10% silver and 90% copper by mass, then based on metal densities and commodity prices, the cost of the cathode will be about $\$0.58/m^2$. If the assume the anode is 400 nm thick and comprised of 100% iridium, the requisite quantity of this metal will cost about $\$281/m^2$. If both the anode and cathode are supported with 0.025 mm thick titanium foil, this will add $\$5.65/m^2$ to the cost (at \$50/kg). The anion exchange membrane costs on the order of \$60 per square meter. We estimate that the mechanical and electrical components – e.g., the cell enclosure, fittings, and the power inverter – will add an additional \$100.

Table S12. Summary of prospective costs of a CO_2 reduction cell.

Components	**Estimated Marginal Cost in USD (per m^2)**
Cathode	\$0.58
Anode	\$281
Electrode support	\$5.65
Anion exchange membrane	\$60
Mechanical and electrical components	\$100
Total (per m^2)	**\$447**
System (for 0.5 m^2 electrolysis cell)	**\$224**

The insolation data from the Mojave Desert in California is used to calculate the production rate of chemicals. The average direct normal irradiance is about 8.021 $kWh/m^2/day$, which translates to 10.54 GJ over the course of a year. This is total energy available for energy conversion. Considering a 20% efficient solar cell and a 30% energetic efficiency to the targeted products for the electrolysis cell, the total converted energy is 632 MJ/year.

We consider two limiting cases. If 100% of the converted energy goes into ethylene, 13.5kg will be produced, worth \$9.08 based on commodity pricing. If 100% of the converted energy goes into ethanol, 20kg will be produced, worth \$25.35 (at the typical bioethanol target price of \$1/L).

This analysis shows that targeted cost reductions are necessary to decrease the device payback time. A prime target for optimization or material substitution is the anode, currently made of iridium. If the anode could be made as cheaply as the cathode, for example by using a bimetallic such as NiFe, the monetary payback time could be under 5 years, bearing in mind the simplifying assumptions detailed above. The anion exchange membrane is another opportunity for cost reduction.

References

1 C. D. Wagner and G. E. Muilenberg, *Handbook of x-ray photoelectron spectroscopy : a reference book of standard data for use in x-ray photoelectron spectroscopy*, Physical Electronics Division, Perkin-Elmer Corp., Eden Prairie, Minn., 1979.

2 S. González, M. Pérez, M. Barrera, A. R. González Elipe and R. M. Souto, *J. Phys. Chem. B*, 1998, **102**, 5483–5489.

3 M. C. Biesinger, B. P. Payne, A. P. Grosvenor, L. W. M. Lau, A. R. Gerson and R. S. C. Smart, *Appl. Surf. Sci.*, 2011, **257**, 2717–2730.

4 C. D. Wagner, D. A. Zatko and R. H. Raymond, *Anal. Chem.*, 1980, **52**, 1445–1451.

5 P. J. Linstrom and W. G. Mallard, *NIST Stand. Ref. Database Number 69*, 2017.

6 *Design Institute for Physical Properties*, AIChE, DIPPR Proj., 2016.

7 D. T. Whipple and P. J. A. Kenis, *J. Phys. Chem. Lett.*, 2010, **1**, 3451–3458.

8 B. A. Rosen, A. Salehi-Khojin, M. R. Thorson, W. Zhu, D. T. Whipple, P. J. A. Kenis and R. I. Masel, *Science (80-.).*, 2011, **334**, 643–644.

9 P. G. Russell, N. Kovac, S. Srinivasan and M. Steinberg, *J. Electrochem. Soc.* , 1977, **124** , 1329–1338.

10 T. Yamamoto, D. A. Tryk, A. Fujishima and H. Ohata, *Electrochim. Acta*, 2002, **47**, 3327–3334.

11 K. Wu, E. Birgersson, B. Kim, P. J. A. Kenis and I. A. Karimi, *J. Electrochem. Soc.*, 2014, **162**, F23–F32.

12 M. Schreier, L. Curvat, F. Giordano, L. Steier, A. Abate, S. M. Zakeeruddin, J. Luo, M. T. Mayer and M. Grätzel, *Nat. Commun.*, 2015, **6**, 7326.

13 D. A. Vermaas and W. A. Smith, *ACS Energy Lett.*, 2016, **1**, 1143–1148.

14 X. Zhou, R. Liu, K. Sun, Y. Chen, E. Verlage, S. A. Francis, N. S. Lewis and C. Xiang, *ACS Energy Lett.*, 2016, **1**, 764–770.

15 C. Delacourt, P. L. Ridgway, J. B. Kerr and J. Newman, *J. Electrochem. Soc.* , 2008, **155** , B42–B49.

16 S. R. Narayanan, B. Haines, J. Soler and T. I. Valdez, *J. Electrochem. Soc.* , 2011, **158** , A167–A173.

17 Y. Kwon, Y. Lum, E. L. Clark, J. W. Ager and A. T. Bell, *ChemElectroChem*, 2016, **3**, 1012–1019.

18 A. ElMekawy, H. M. Hegab, G. Mohanakrishna, A. F. Elbaz, M. Bulut and D. Pant, *Bioresour. Technol.*, 2016, **215**, 357–370.